Visual pathway origins: an electron microscopic volume for connectomic analysis of the human foveal retina

Yeon Jin Kim[1], Orin Packer[1], Thomas Macrina[2], Andreas Pollreisz[3], Christine A. Curcio[4], Kisuk Lee[2], Nico Kemnitz[2], Dodam Ih[2], Tri Nguyen[2], Ran Lu[2], Sergiy Popovych[2], Akhilesh Halageri[2], J. Alexander Bae[2], Joe Strout[2], Stephan Gerhard[5], Robert G. Smith[6], Paul R. Martin[7], Ulrike Grünert[7], Dennis M. Dacey[1,8,9,*]

[1]Department of Neurobiology & Biophysics, University of Washington, Seattle, WA, 98195

[2]Zetta AI LLC, Sherrill, NY, USA

[3]Department of Ophthalmology, Medical University of Vienna, Vienna, Austria

[4]Department of Ophthalmology and Vision Sciences, University of Alabama at Birmingham, Alabama 35294

[5]Aware LLC, Rappenstrasse 19, 8307 Effretikon, Switzerland

[6]Department of Neuroscience, University of Pennsylvania, Philadelphia, PA 19104

[7]The University of Sydney, Save Sight Institute and Discipline of Ophthalmology, Faculty of Medicine and Health, Sydney, NSW, 2000, Australia

[8]Washington National Primate Research Center, Seattle, WA 98195

[9]Lead contact

*Corresponding author: Dennis M. Dacey (dmd@uw.edu)

This file includes:

Main Text (Main text pages: 21, Total pages: 67)

Figures 1 to 7

In Brief (currently 36 words)

Deep-learning based reconstruction of cells and synapses in a human fovea reveals visual pathway origins and human-specific wiring for color vision, opening the door to a complete synaptic-level connectome of this critical locus in the human central nervous system.

Highlights

- Complete EM level reconstruction of cells and synaptic circuitry in a human fovea
- New circuit motifs for short-wavelength (S-cone) pathways feeding color vision
- Pathways to the brain are greatly reduced relative to non-primate mammals

Summary

With over 10^{14} synapses, the human brain presents a seemingly insurmountable challenge to a nano-scale circuit-level understanding of its diverse neural systems. The foveal retina however presents a feasible site for a complete connectome of a key human CNS structure. Foveal cells and circuits are miniaturized and compressed to densely sample the visual image at highest resolution to initiate form, color and motion perception. Here we use computational methods first applied to the fly brain to provide a draft connectome of all neurons in a foveal volume. We found synaptic connections distinct to humans linking short-wavelength sensitive cones to color vision pathways. Moreover, by reconstructing excitatory synaptic pathways arising from cone photoreceptors we found that 96% of foveal ganglion cells contribute to only three major pathways to the brain. This new resource reveals unique features of a human neural system and opens a door to its complete connectome.

Keywords: Human CNS, Human fovea, Human retina connectome, Human Müller cells, Human bipolar cells, Human ganglion cells, Human amacrine cells, Human microglia, Human astrocytes, Human color vision.

Introduction

The vertebrate retina was one of the first neural structures where the great complexity of neurons and their circuits was recognized[1], and where critical links were later made between cell structure and visual function [2,3]. The retina was also a focus of early application of connectomics methods to reconstruct neural systems at the synaptic level [4-9] and most recently has emerged as a system where anatomically and functionally distinct cell populations can be linked to their molecular profiles [10-13] and the genetics of human disease [12,14]. Yet even for this intensively studied, most accessible part of the central nervous system (CNS), the number of cell types – on the order of 100 – that may synaptically interact has precluded a full wiring diagram of how one of our most fundamental senses, vision, is initiated.

The recent achievement of a complete connectome of the brain of the fruit fly, Drosophila melanogaster [15,16], has made the connectome of a larger mammalian brain a now-conceivable goal [17-20] and connectomic methods have now been applied to mm scale volumes of mouse and human neocortex [18,19,21,22]. Nanoscale analysis of the neocortex is overwhelmingly hampered by the many input and output pathways that cannot yet be identified while a human brain connectome remains an immense challenge for each of its many neural systems. In the present study we take advantage of the specialized properties of the foveal retina to provide a first draft connectome of this critical locus in the human CNS.

The fovea is a specialized central region in the retina of humans and other day-active primates ideally suited to the connectomics approach where, like a miniature brain, neural circuits are spatially compressed to facilitate highest resolution form, color and motion perception. At barely 1 mm wide the fovea encodes the central few degrees of visual space, but its representation is magnified 100-fold across the surface of primary visual cortex [23-27] making it essential for perception. Failure of foveal function is a hallmark of the most devastating blinding retinal diseases.

From a signal-processing viewpoint, the retina is a self-contained input-to-output sensory structure where light transduction by photoreceptors is processed by diverse neural cell types occupying two cell and synaptic layers across a physical span of just ~200 µm. The foveal volume presented here thus houses complete arrays of parallel visual pathways from sensory receptor to output neuron. We provide an inventory of all foveal cell types and their relative numbers, as well as the assignment of synaptic connections to characterize functional circuits. We directly address the long-standing question of the number and identity of visual pathways that link the fovea to the brain. We find only three major visual pathways accounting for about 96% of the projection to the human brain: a striking reduction compared to both non-primate mammals [28-30] and non-human primates [31,32]. Lastly, initial exploration of cell type specific circuits indicates that the neural coding for trichromatic color vision may be specific to our own species. This human foveal dataset is now available to an open community of users to finalize the connectome and model its functional properties.

Results

Acquisition of the foveal volume. Our goal was to obtain complete retinal circuitry near the peak of cone density (peak of visual acuity) [33,34]. The task is complicated because foveal cones feed inner retinal circuits via very long axons (Henle fibers, Figures 1A-1C) [35]. Our ROI therefore was taken at 500 µm from the foveal center, where cone axon length averages 400 µm [36]; this ROI location is linked to cones located ~100-300 µm from the pit center (~0.7-1.4 deg). We cut 3028 vertical sections at 50 nm through a total depth of ~150 µm and imaged an area that was 180 µm tall x 180 µm wide (5 nm pixels) extending from the Henle fiber layer at its outer border to the nerve fiber layer at its inner border (Figure 1D). We used recent computational methods [37,38] to align the images, detect membrane boundaries, segment neurons and glia, and finally to detect synapses (Figures 1D-1K; see Star Methods for details). For ease of reference, we named this volume HFseg1 (Human Fovea, segmented 1). The initial segmentation was used to proofread, annotate and type all cells in HFseg1 (Figures 1F-1G; see Table S1A, 3008 total cells). All cell types and draft synaptic connections are available in an accessible form at NeuroMaps (https://neuromaps.app/datasets, see Table S3).

Cell populations

Non-neuronal cells. Müller cells are radial glia with cell bodies in the INL and processes that extend from the external (photoreceptor inner segment-ONL border) to the internal limiting membrane (Figure S1A). We could readily annotate all Müller cells (555 cells, Figure 1G, Table S1B) because their nuclei were distinctly large and strictly euchromatic (Figures S3C, S3F). A second, smaller population of glial cells was present in the GCL (Figures S1B, S3B) and provisionally identified as astrocytes [39] (32 cells, Table S1B). These cells showed cell bodies that

118 apposed blood vessels and sparsely branched dendrites that radiated from the soma without
119 penetrating the INL (Figure S1B).

120 Lastly, we identified 15 microglial cells (Table S1B) with cell bodies in the IPL or GCL (Figure
121 S1A); a few cells were also associated with the deep retinal vasculature at the OPL-INL border.
122 They show nuclear morphology (Figures S3A) distinct from both Müller cells and astrocytes
123 (Figures S3C, S3B). The density of microglial cells was low, consistent with previous
124 measurements in the macaque monkey foveal retina [40,41].

125 ***Photoreceptors.*** HFseg1 contained 313 cone (pedicles) and 24 rod (spherules) synaptic
126 terminals (rod : cone = 0.07, Tables S1C, 1D). Rods first appear ~100 μm from the foveal center
127 [33,34,42]. Fifteen cone pedicles were identified as short wavelength sensitive (S) cones (Table S1C,
128 Figure 2A) based on distinctive connectivity [43]. The remaining 298 cones comprised long (L) and
129 medium (M) wavelength sensitive cones, referred to collectively as LM cones.

130 Cone pedicles contact each other by short extensions (telodendria) or by distinct pedicle-to-
131 pedicle apposition (Figure 2B). These contacts harbor gap junctions representing the earliest
132 neuronal interactions in the visual pathway. In non-human primates, LM–LM cone contacts are
133 abundant, but S–LM contacts are greatly reduced or absent [43,44], apparently reflecting a need to
134 support color vision by isolating short from long wavelength signals [45,46]. In human retina
135 however S-LM cone contacts are reported [47,48]. We therefore mapped the full cone-cone
136 connectivity to determine whether S-LM contacts are a consistent feature of human fovea. We
137 used automated methods to detect all cone-cone contacts (n = 1141 contacts). Contacts were
138 large with a thick, darkly stained region defining the contact area (see Figure 2B insets) [49]. We
139 found abundant S–LM cone contacts (n = 15 S cones; 4.93 ± 1.91 contacts/*pedicle*), with LM–LM
140 cone contacts (n = 298 LM cones, 6.90 ± 3.07 contacts/*pedicle*) occurring at somewhat higher
141 frequency.

142 ***Horizontal cells.*** The horizontal cell network in the outer retina generates lateral negative
143 feedback that contributes to the antagonistic receptive field surround of cones, bipolar cells, and
144 ganglion cells. In macaque retina the horizontal cell mediated surround is required for color-
145 coding light responses [50-52] and is therefore a key element in the circuitry that initiates color
146 vision. Two horizontal cell types, H1 and H2 cells, with distinctive morphology and cone
147 connectivity, are widely recognized in peripheral primate retina [53-57]. Knowledge of the horizontal
148 cell populations in the foveal human retina remains rudimentary though H1 and H2 cells have
149 been distinguished by immunostaining[58], morphology [43] and in transcriptomic datasets [12].

150 We annotated 265 horizontal cells in HFseg1 and found almost all (255 cells) to be H1 cells
151 (Table S1E) with a very small population of the H2 cells (10 cells). The H1 cells showed small
152 (~30–50 μm diameter) and profusely branched dendritic trees. Neighboring H1 cells overlapped
153 extensively such that each cone pedicle was contacted by several H1 cells (Figures 2C and 2C
154 insets). For most cells a long axon-like process arose from the soma or dendrite and extended to
155 the edge of the volume within the OPL without branching (indicated by arrows, Figure 2C; these
156 long processes are known to terminate in a finely branched arbor that innervates rod spherules
157 [59,60]). In contrast to H1 cells, the H2 cells showed very large, and loosely branched dendritic trees
158 (>100 μm in diameter) that only sparsely innervated most cone pedicles and showed little
159 dendritic overlap with neighboring H2 cells (Figure 2D). Consistent with previous descriptions,
160 the axon of the H2 cells was meandering and made additional sparse contacts with cone
161 pedicles [54-56].

162 In macaque and marmoset retina H1 cells largely avoid contact with S cones whereas H2 cells
163 show some selectivity for S cones [55,57,61]. The substantially higher density of H1 cells relative to
164 H2 cells in HFseg1 altered this expected synaptic relationship. We found the H2 cells do
165 maintain some preference for synapsing with S cones (Figure 2D). However, we also found that
166 the numerically dominant H1 horizontal cells formed most synapses with S cones (H1, 86.3%

167 ±1.8%; H2, 13.8% ± 1.8%, n = 2 S cones). In addition, H2 cells formed less than 2% of the
168 horizontal cell contacts with two identified LM cones (H1, 98.1% ± 0.1%; H2, 1.9% ± 0.1%, n = 2
169 LM cones) (also Figure S4). The H1 cells therefore receive input from and are expected to
170 provide negative feedback to all three (S, L and M) cone types (Figures 2C, 2D and S4). Taken
171 together, the S-LM cone coupling and the combined S and LM cone connectivity of H1 horizontal
172 cells provides new connectomic evidence for a difference between human and non-human
173 primates in color related circuitry[43] that can now be explored in greater depth in HFseg1.

174 ***Bipolar cells.*** In foveate primates, flat (FMB, OFF type) and invaginating (IMB, ON Type) midget
175 bipolar cells show dominant connections to single cones and ganglion cells, whereas diffuse
176 types contact several cones and have been divided into 8 types (DB1, 2, 3a, 3b, 4, 5, 6 and
177 Giant) [62]. Finally, a single blue cone bipolar (BB) cell type shows selective targeting of S cones.
178 We annotated 912 bipolar cells (Table S1F); the major types recognized in non-human primates
179 were identified but with some notable differences outlined below (Figure 3).

180 Of the cells with distinctive cone connectivity, FMB (302 cells, Table S1F) and IMB cells (264
181 cells, Table S1F, Figures 3A, 3B) accounted for 62% of all bipolar cells. Blue-cone bipolar cells
182 (BB cells; Figures 3B, 3C, S5) by contrast formed only 1.9% of all bipolar cells (17 cells, Table
183 S1F). All ON bipolar cells showed darkly staining, heterochromatic nuclear profiles that
184 distinguished them from most other cells in the INL (Figure S3F). Of the presumed OFF diffuse
185 bipolar types we identified DB1 [63] (54 cells), DB2 (92 cells) and DB3 (41 cells, Table S1F,
186 Figures 3A, 3C) types, each formed distinctive axonal mosaics. We were not able to divide the
187 outer DB3 cells into the previously identified DB3a, DB3b types [64-67]. The DB3 cells showed large
188 axonal fields and likely correspond to the calbindin-positive DB3a type in macaque, marmoset
189 and human retina [68-71]. If this association holds then DB3b cells are either absent or present at a
190 very low density in the foveal DB population.

191 In the inner half of the IPL, DB4 (34 cells), DB5 (45 cells) and DB6 cells (12 cells, Table S1F)
192 were distinguished by axonal morphology and stratification depth (Figures 3B, 3C). We failed to
193 observe a clear correlate of the more recently described Giant bipolar type [72,73] but a small
194 number of unidentified cells that remain to be studied in detail could include the Giant type (n = 7,
195 Table S1F). Lastly, rod bipolar cells (RB, 6 cells, 0.7% of total BCs, Table S1F) made
196 invaginating contacts, as expected [74,75], with the small number of rod spherules and showed
197 small unbranched axonal arbors that contained far fewer ribbon synapses (15.8 ± 2.2 ribbons, n
198 = 5) than diffuse or midget bipolar cells (see Figure S10) [76,77].

199 Bipolar cells not previously described in primates were also present in HFSeg1. One group
200 showed small field amacrine-like morphology (called here outer-x and inner-x in Figures 3A, 3B)
201 but nevertheless contained abundant ribbon synapses (Figure S6). Similar cells were found
202 recently in mouse retina [10,78] and likely correspond to the OFF-x bipolar cells identified by
203 transcriptomics of human fovea [12] (20 cells, Table S1F). While most of these cells stratified in the
204 outer half of the IPL (Outer-x cells, n = 15, Figures S6A-S6B), 5 examples stratified in the inner
205 half of the IPL (Inner-x cells, Figures S6C-S6G). Another previously undescribed bipolar type
206 showed the typical DB cell connection to cones but extended axonal branches in both outer and
207 inner IPL to varying extents. We referred to this cell group as DBbroad (18 cells, Figures 3A, S7,
208 Table S1F). The exact connections of these cells remain to be determined but we observed
209 synaptic output to OFF-outer and ON-inner ganglion cell types (see also Figures S7C, S7E). In
210 the OPL, DBbroad cells made only basal contacts with cone pedicles and thus we have placed
211 the DBbroad cells provisionally in the OFF bipolar category, though the lack of invaginating cone
212 contacts does not preclude an ON-type response from these cells [79].

213 In sum, the bipolar cells in HFseg1 could be related to previous classification of midget and
214 diffuse bipolar types for non-human primate retina. However, some bipolar types appeared
215 absent or very low in density (DB3b and Giant types) or not previously observed (DBbroad, x-

216 type). Our classification can now be substantiated or modified by a more complete analysis of
217 synaptic connectivity.

218 ***Amacrine cells.*** We identified 293 amacrine cells, including 40 cells displaced to the ganglion
219 cell layer (Table S1G). Most amacrine cells showed cell type-specific nuclear staining (from
220 strongly heterochromatic to strongly euchromatic) and nuclear shape (from smooth and round to
221 deeply infolded) (Figure S3).

222 We sorted the amacrine cells into small (diameter < 100 μm; n = 189), and large field (diameter
223 >100 μm) groups (n = 104). We divided these groups into 19 types (6 small field and 13 large
224 field; Table S1G) based on morphology, stratification, mosaic interactions and nuclear
225 morphology (Figures S3, S8, S9). Figure 4 provides a partial view of this dataset by highlighting
226 four cell types (see also Table S3); two additional amacrine populations are illustrated in Figure
227 S8.

228 The AII type (AC2) was present at the highest density of any amacrine cell population (75 cells,
229 Table S1G). This cell type was recognized by its well-established morphology across species [80]
230 including human [62,81,82] (Figures 4A, 4B). A major function of AII cells is to transfer signals from
231 rod bipolar to cone bipolar cells, serving as conduits for rod signals to ganglion cells at scotopic
232 light levels [83]. However, the presence of AII amacrine cells at such a high density in the fovea,
233 where rods are all but absent, suggests a circuit function switch to a primary role in photopic
234 spatial vision. Indeed, we observed that AII cells in HFseg1 are postsynaptic to varied cone
235 bipolar types, including IMB cells (Figure S9).

236 The second amacrine type highlighted here (Figures 4C, 4D) is the starburst amacrine (17 cells,
237 AC7 (SAC) in Table S1G). Starburst cells have been intensively studied in mouse and rabbit
238 retina for their pivotal role in direction selectivity in ganglion cells [84] and are present in primate
239 retina, including human [12,85-87] , though their connectivity and contribution to direction selectivity

240 in foveal retina is unknown. Almost all starbursts were found in the ganglion cell layer (GCL),
241 where they were the most numerous AC type (14/40 cells, 35%, see lower panel in Figure 4D),
242 consistent with previous estimates [85,87].

243 An additional small field type, AC11 (22 cells, Figures 4E, 4F, Table S1G) showing fine, densely
244 branched, broadly stratified dendrites falls into a group of cells conventionally referred to as
245 "knotty" amacrines [88-90] and may correspond to the strongly parvalbumin positive cells described
246 in macaque monkey [91]. By contrast the large field type, AC8 (10 cells, Figures 4G, 4H, Table
247 S1G) shows thick, narrowly stratified, radiate dendrites that are both pre- and postsynaptic to
248 FMB axon terminals.

249 In sum, the HFseg1 volume will now make it possible to directly determine the complete
250 connectivity of each of the amacrine types as a framework for understanding their roles in foveal
251 function.

252 **Evaluation of synapse detection.**

253 To assess the accuracy of ribbon segmentation and synapse prediction (Figures 1H-1K), we
254 compared predicted synaptic assignments to manual (ground truth) assignments. We focused on
255 the incoming cone-to-midget bipolar cell synapse in the OPL and the outgoing midget bipolar cell
256 synapses to amacrine and ganglion cells in the IPL. For ground truth, we manually annotated
257 these connections for the ON and OFF midget pathways linked to three LM cones (cones 21, 22,
258 and 58; Figure S10, Tables S2A-S2C).

259 Figures 5A-5B show the predicted outgoing synapses for a pair of midget bipolar cell axon
260 terminals. Measures of precision (true synapses/[true synapses + false positives]) and sensitivity
261 (true synapses/[true synapses + false negatives]) were taken for ribbon identification and
262 synaptic partner assignments. The predicted segmentation of ribbons showed precision and
263 sensitivity near 100%; there were few false positives and nearly zero false negatives (precision:

264 93.5% ± 2.7%; sensitivity: 99.7% ± 0.8%, n = 6 midget bipolar cells, 370 total ribbons, Figure 5B
265 inset). Synaptic assignment for these ribbons was also excellent (precision: 89.0% ± 5.4%;
266 sensitivity: 93.7% ± 4.6%, n = 6 midget bipolar cells, 637 total synapses, Figure 5B inset). These
267 values demonstrate for the first time the high accuracy of convolutional nets for predicting and
268 segmenting ribbon synapses.

269 By contrast with the ribbon synapses made in the IPL, ribbon synapses made by the cone
270 pedicle are extremely complex [92,93] (Figures 1H, 1I). Crucially, synaptic processes can either
271 invaginate into the synaptic face of the pedicle to reach the active zone or occupy a basal (or flat)
272 position at base of the cone pedicle up to ~800 nm from the sites of transmitter release [93,94].
273 Bipolar cells form type-specific connection motifs with the cone pedicle [66,72,93] so we determined
274 not only whether a synapse was predicted, but also how well the number of incoming synapses
275 from a cone to a specific bipolar cell type was captured. We mapped all incoming cone synapses
276 to the dendritic tips for each of six midget bipolar cells sampled. We found high precision and
277 sensitivity for ribbon detection (n = 51) in the 3 cone pedicle (precision: 92.3% ± 6.7%; sensitivity:
278 100% ± 0%, n = 3 LM cones, Figures S2A-S2C) and for the multiple postsynaptic processes (n =
279 153) deriving from the invaginating (IMB) and flat (FMB) midget bipolar cells (precision: 98.7% ±
280 1.2%; sensitivity: 99.7% ± 0.6%, total synaptic connections, see Figure S2C right). Diffuse
281 bipolar cells, which make more sparse connections with multiple cones, were also sampled (n =
282 2, DB4 and DB2; Figures S2D-S2F), yielding similar precision and sensitivity results.

283 For inhibitory synapses we focused on the dominant AII amacrine cell (Table S1G) where a
284 glycinergic synapse to OFF bipolar cells is well established [80,81,95,96]. We manually mapped all the
285 outgoing synapses made by two neighboring AII amacrine cells and compared our ground truth
286 data to the predicted synaptic assignments (Figures 5C-5G). The prediction captured well the
287 origin of synaptic output from the outer stratifying lobular appendages of the AII cell to outer-OFF
288 bipolar cells (Figures 5D-5G). Vesicle clouds were also detected with high sensitivity (87.5% ±

289 0.7%, n = 2 AIIs; false negatives were rare, Figure 5C bottom) but relative to ribbon detection,
290 there were more false positives, thereby reducing the accuracy of the overall synapse detection
291 (76.0% ± 8.5%, n = 2 AIIs). With this limitation, the results show that our dataset accurately
292 reflects synaptic connectivity and can serve as a starting point to build a complete synaptic level
293 connectome of foveal human retina.

294 ***Ganglion cells.*** We annotated 599 ganglion cells (Table S1H). Thirteen GCs were displaced to
295 the INL or IPL. Midget GCs comprised the great majority (536 cells, ~90%, Table S1H) [12,97] and
296 were readily divided into outer-OFF stratifying (280 cells) and inner-ON stratifying (256 cells)
297 types (Figures 6A, 6E). A second well defined cell type, the parasol cell (26 cells, 13 inner-ON
298 cells and 13 outer-OFF cells, ~4% of total GCs) was also easily distinguished (Figures 6B, 6F,
299 Table S1H). Small bistratified GCs (12 cells, ~2% of total GCs, Table S1H), were distinguished
300 by their broad dendritic ramification (Figures 6C, 6G) and extensive synaptic input from blue
301 cone bipolar cells (BB cells) [98]. Together, the midget, parasol and small bistratified cells account
302 for 95.8% of the ganglion cell in HFseg1. The remaining 25 ganglion cells show relatively large
303 dendritic fields, various morphological forms and, taken together, should constitute all remaining
304 central visual pathways present at this retinal location.

305 We divided these remaining cells into 6 provisional types of large field GCs. Large field GC1
306 (LFGC1, 6 cells, Table S1H) was postsynaptic to blue-cone bipolar cells and a dendritic tree that
307 co-stratified with the small bistratified cells (Figures 6D, 6H). These cells likely correspond to the
308 large bistratified GC observed in the human fovea [47] and marmoset and macaque retinal
309 periphery [31,99]. Large field GC2 (LFGC2, 6 cells Table S1H) showed broadly stratified and
310 densely branched dendritic trees (Figures 6I, 6L); a counterpart in monkey retina remains
311 unclear but similar morphology has been observed in human peripheral retina [100]. A third cell
312 group (LFGC3, 4 cells, Table S1H) stratifies across the center of IPL (Figures 6J, 6M) and
313 appears to correspond to previously described recursive bistratified cells, identified as ON-OFF

direction selective cells in the macaque monkey retina [32]. A fourth cell group (LFGC4, 5 cells, Table S1H) shows large cell bodies and radiate dendritic branching near the center of the IPL costratified with the inner-ON and outer-OFF parasol cells (Figures 6K, 6N) (3 inner and 2 outer stratified) and could correspond to the smooth mono-stratified type identified in macaque and marmoset retina [31,32,101]. A fifth group of cells (not shown) shows very sparsely branching dendrites stratified in the inner IPL (LFGC5, 4 cells, Table S1H) that could correspond to inner melanopsin cells (or an inner sparse type recognized in macaque and marmoset). Lastly, a few very sparsely branching GC processes (not linked to cell bodies within the volume) were very sparsely branching and stratified along the outer border of the IPL were also present, likely corresponding to outer melanopsin ganglion cells [102]. If included in our current total this would give 7 large field types and 12 ganglion cell types in total.

Our provisional classification shows multiple ganglion cell types observed in the monkey and human retinal periphery absent from HFseg1 and, by implication from the normal human fovea. This result also stands in sharp contrast to the retina of the mouse where ~40 GC types have been distinguished throughout the retina [28-30]. To this point however we had not ruled out the possibility that cell bodies of some ganglion cell types are not present in the volume but have large dendritic trees which penetrate the volume and contribute significantly to the circuitry of the inner retina. We therefore took a second approach to identifying the visual pathways in HFseg1 by mapping what we called the “vertical excitatory connectome”.

The vertical excitatory connectome

We reasoned, as others have [103], that to generate parallel pathways to the brain each cone must be locally presynaptic to each cone bipolar type (for the S cone, there is uncertainty on this point, due to its more specialized role in color vision). At the next synaptic step, the total output of all bipolar cell types should project to all ganglion cell types. In other words, in principle, *all visual pathways should be synaptically linked to the output of any given cone*.

339 To test this hypothesis, we annotated the ribbon synapses and all postsynaptic bipolar cells for
340 three LM and two S cones. For each bipolar cell the synaptic ribbons and their postsynaptic
341 targets were next identified (Figures 7A-7B). For each ribbon synapse we then identified the
342 postsynaptic GC partner(s). Finally, we determined the relative synaptic density from a given
343 cone via its postsynaptic bipolar cells to each identified GC (see details in Figures S10-S11 and
344 Table S2).

345 We found that bipolar cells connected to the three LM cones synapsed overwhelmingly with
346 midget and/or parasol ganglion cells (Figure S10), accounting for 92.1% of the total bipolar
347 synaptic output *to ganglion cells* (Figures 7C, 7D, S10, Tables S2A-S2C). Thus, synaptic density
348 mirrors well the cell density (midget and parasol cells together account for 93.8% of all ganglion
349 cells in HFseg1, Table S1H). By contrast, the large field ganglion cell types (LFGC1-LFGC5,
350 Figures 6D, 6H, 6I-6N) identified in our GC survey (Figure S10, Tables S2A-S2C) received 7.9%
351 of the bipolar synaptic output, while accounting for 4.2% of the total ganglion cells (Table S1H).
352 Output to dendritic fragments of unidentified ganglion cells was rare, accounting for ~0.5% of the
353 total bipolar output to ganglion cells (0.53 ± 0.76, n = 3 LM cones, Tables S2A-S2C). These data
354 align with our population analysis described above and show that, for the LM cones, diverse
355 synaptic signals are overwhelmingly targeted to the midget and parasol pathways, with the
356 remaining 5-10% of synapses distributed across a limited number of large field, very low density
357 pathways.

358 One final unanticipated feature of the HFseg1 dataset stands out, that is, a striking asymmetry in
359 the bipolar output (Figure 7C), with about twice the number of ribbon synapses arising from OFF
360 pathway connections. For example, 595 excitatory synaptic contacts are directed at OFF parasol
361 cells, compared to 233 synapses directed at ON parasol cells (n = 5 cones): a greater than
362 twofold difference. This result provides a plausible synaptic basis for the well documented

363 dominance of OFF pathway processing in human vision [104-106] and at higher levels in the visual
364 pathway [107,108] and can now be explored further in the HFseg1 connectome.

365

366 **Discussion**

367 **A human foveal connectome.** Our aim was to apply computational tools developed to
368 reconstruct and proofread the Drosophila nervous system [15,16,109] to generate an accessible
369 dataset enabling the first connectome in the human CNS. The current dataset includes
370 segmentation of all cells and other membrane bounded structures as well as identification of
371 synapses and synaptic partner relationships. Given ~2400 neuronal cell bodies in the volume
372 already typed, ~25k edits already made, and a mean additional proofread time of 30
373 minutes/neuron we estimate ~1200-person hours for proofreading to completion. Thus, with a
374 relatively small number of users engaged by specific circuit hypotheses, the HFseg1 connectome
375 could be completed in less than six months.

376 **Cell type profiling.** HFseg1 permitted a provisional identification all cell types and their relative
377 densities (Table S1). Similar datasets currently exist for large cell samples from human and non-
378 human primate central retina where cell types were clustered by gene expression profile and
379 linked to anatomical types by marker genes [11,12,14,110,111]. HFseg1 permits a comparison of the
380 two approaches and suggests generally good correspondence though with some unexpected
381 differences. For example, the ratio of H1 to H2 horizontal cell types identified by transcriptomics
382 were shown in macaque and human central retina to be ~3:1 and 7:1 respectively. By contrast
383 our connectomic profile shows that the H1 to H2 ratio is much higher (26:1) with H1 cells forming
384 96.2% of the horizontal cells at this foveal location. Thus, the transciptomically-identified trend
385 towards the H1 cell type in the fovea is evident but much more extreme in HFseg1. A similar
386 trend holds for other clearly identified types: midget ganglion cells make up ~90% of the ganglion

387 cell population in our sample and 86% in the transcriptome; AII and starburst amacrine cells
388 make up 26% and 5.5% of the amacrine cell population respectively but only 18% and 1.3% of
389 the amacrines identified by molecular profiling. Conversely parasol ganglion cells account for
390 only 4.4% of HFseg1 ganglion cells but 10% in a transcriptomics sample [12]. One explanation for
391 these differences may be that our smaller sample represents the cone-enriched foveal center
392 whereas the larger samples used for single cell RNAseq encompassed a much larger area (~1.5
393 mm, central 5 degrees) of central retina; cell type-specific density changes are extremely steep
394 across this region and the larger spatial sample would average out such changes.

395 Certain cell populations previously recognized have not, at least thus far, been evident in
396 HFseg1. For example, the recent functional, anatomical and molecular distinction made between
397 diffuse bipolar types DB3a and DB3b in macaque monkey [65,66] and human retina [12,69] was not
398 apparent in HFseg1. Though provisional, we found evidence for only 19 amacrine cell
399 populations whereas molecular profiling proposes 73 amacrine cell types in human retina [14]. This
400 difference suggests that the relationship between cells defined by gene expression and
401 anatomical types may not always be straightforward (with the caveat noted above that tissue
402 location may impact the relative densities (and corresponding circuitry) of cell populations).

403 **The vertical excitatory connectome.** In the retina of the mouse ~40 distinct ganglion cell
404 populations have been recognized [28-30]. In non-human primate fewer than 20 pathways have
405 been defined, with transcriptomic and anatomical identification in reasonable agreement [11,31,32].
406 In human fovea, only 12 pathways have been suggested by transcriptomic analysis [12,14] in close
407 agreement with the current results. It was nevertheless striking that in the HFseg1 dataset ~96%
408 of the ganglion cells comprised just 3 anatomically distinct groups: the midget, parasol and small
409 bistratified cells. When we manually traced the vertical connectome from a single cone to its
410 postsynaptic bipolar cells and in turn to all postsynaptic ganglion cells we obtained the same
411 result, with these three major pathways accounting for over 90% of the synapses from bipolar

412 cells to ganglion cells. Thus, the reduction in the number of visual pathways appears to be a
413 fundamental, defining feature of foveal synaptic organization. A simple explanation might be the
414 need to transmit a high-fidelity signal with single cone resolution, with the required midget
415 ganglion cells in essence squeezing out all the other ganglion cell types. But there are other
416 major changes in the connectome related to foveal function that remain to be understood. For
417 example, rod photoreceptors are absent or greatly reduced at the foveal center, but how this
418 might impact overall visual pathway cell type diversity and function is unknown. Similarly, the
419 number of directionally selective visual pathways found in non-primate mammals appears greatly
420 reduced in non-human primates [32,112] but the significance of this difference remains to be
421 clarified.

422 **The foveal connectome and human color vision.**

423 Most psychophysically based models of human color vision assume the presence of two parallel
424 color opponent channels: red vs green and blue vs yellow [109]. The red-green pathway shows
425 opposing L vs M cone interaction and has been associated with the circuitry that feeds the
426 midget ganglion cell [113]. However, the human psychophysically defined red-green pathway
427 requires that a small S cone input also be incorporated[114]. The locus of this critical synapse
428 remains unclear with recent data from macaque monkey implicating both retina [110] and primary
429 visual cortex [111]. The HFseg1 connectome shows that H1 horizontal cells, a major source of the
430 surround in the midget circuit [51], likely contribute antagonistic signals from L, M and S cone
431 types, thereby providing a simple and unanticipated explanation for the added S cone
432 contribution to the human red-green channel. An interaction site early in S, L and M cone
433 pathways of the human fovea might also begin to explain unexpected S-LM cone coupling, i.e.,
434 to inject a relatively small high-fidelity S-cone signal into downstream pathways utilized for
435 trichromatic color vision [115,116].

436

Limitations to the study

The HFseg1 dataset reflects the nascent field of comparative connectomics both within and across species. One criticism of connectomics is small sample size [20] which can impact interpretation of the connectome, even for the relatively stereotyped fly brain [117], and more so for the highly variable human nervous system. However, because the fovea is small it can be replicated in multiple individuals and provide a source for understanding connectomes that vary in visual capacity, age, and health. These considerations aside, the HFseg1 dataset suggests extreme differences in human foveal retina compared to non-primate mammals, likely reflected in genetic differences in cell types and synaptic connections [13]. A deeper understanding of human connectomes should permit animal models to be better placed into the context of the human nervous system.

Acknowledgements

This work was supported by NIH grants EY-028282 and RF1-MH129260 to D.M.D. and NIH grant P51 OD010425 to the Washington National Primate Research Center and EY01730 to the Vision Research Core at the University of Washington. We thank Sharm Knecht for tissue preparation and managing EM data acquisition.

Author contributions

Y.J.K. and D.M.D. conceived the project. Y.J.K. and D.M.D. generated the ground truth for segmentation and synapses, performed proofreading and created annotations. Y.J.K. and D.M.D. analyzed the data and generated figures. Y.J.K., D.M.D., P.R.M., and U.G., wrote the paper and consulted on figure development. C.A.C. and R.G.S., edited the paper. A.P. acquired human tissue. D.M.D., Y.J.K., C.A.C. and A.P. acquired funding. Zetta AI performed EM data alignment, segmentation, synapse detection and cone-cone contactome detection and ingested all data into the CAVE infrastructure for proofreading. S.G. developed 3D visualizations and analysis tools at NeuroMaps.app.

Declaration of interests

K.L., N.K., D.I., T.N., R.L., S.P., A.H., J.A.B., J.S. and T.M. declare financial interests in Zetta AI.

S.G. is owner of Aware LLC and developed the NeuroMaps.app. The remaining authors declare no competing interests.

469 **Figure legends**

470 **Figure 1. The HFseg1 volume**. **A.** The fovea forms a pit in the retina ~3 mm temporal to the
471 optic disc (within the inset rectangle). **B**. Schematic foveal pit showing cone (red) to bipolar cell
472 (blue) to ganglion cell (green) circuit. ONL, outer nuclear layer, HFL, Henle fiber layer; INL, inner
473 nuclear layer; GCL, ganglion cell layer. **C**. Trimmed retinal block face and ROI (yellow box) in
474 temporal retina ~400 µm from the foveal center. **D**. Single section from the imaged volume
475 (cropped laterally) to illustrate the retinal layers, HFL, OPL, outer plexiform layer; INL; IPL, inner
476 plexiform layer, GCL and NFL, nerve fiber layer. **E**. Volume segmented into membrane bound
477 objects. **F**. Examples of segmented cells photoreceptor axon terminal (PC, white), horizontal cell
478 (HC, orange), ON and OFF bipolar cells (BC, light and dark blue), Müller glia cell (MC, yellow),
479 amacrine cells (AC, green), ON and OFF ganglion cells (GC, dark and light violet); astrocytes
480 and microglia not shown here. **G**. Numbers and cell soma locations of the cell types shown in **F**.
481 **H.** Three segmented ribbons (varied colors) at synaptic triads (red arrowheads) in a single cone
482 pedicle. **I.** Synaptic assignments associated with each ribbon (yellow dots and lines). An IMB
483 (inner-ON midget bipolar; violet, white open arrowhead) cell makes an invaginating contact and
484 two FMB cells (outer-OFF midget bipolar; light and dark blue, white open arrowheads) make a
485 basal contact with the cone pedicle. **J.** Examples of ribbon and synapse prediction in the inner
486 plexiform layer (IPL) for an FMB cell axon terminal at two locations (left and right panels).
487 Segmented ribbons (varied colors, red arrowheads) and synaptic predictions (blue dots, lines).
488 **K.** Inhibitory vesicle cloud segmentation (varied colors) and synaptic prediction (red dots and
489 lines) in the IPL between an amacrine cell and an FMB axon terminal. Insets in **J** and **K** show
490 zoomed view of synapses indicated by white boxes.

491

492 **Figure 2. Photoreceptor and horizontal cell populations**. **A**. Array of photoreceptor axon
493 terminals (cone pedicles, rod spherules) viewing the synaptic face of the terminals (298 LM
494 cones, gold; 15 S cones, blue, 24 rods, brown) (see Tables S1A, S1C, S1D). **B**. Six cone
495 pedicles within the white dotted box in **A**. Left, the pedicles contact each other via telodendria
496 (e.g., arrows) within the circled areas. A pedicle identified as an S cone (white asterisk) contacts
497 neighboring LM cone 230. Right, EM micrographs showing telodendritic contacts (open white
498 arrowheads) between LM cones (top) and S cone with LM cone (bottom). **C**. Six overlapping H1
499 cells are shown (varied colors); each H1 cell forms lateral elements in S cone 15 (blue). Upper
500 inset shows the cell bodies of the six H1 cells. Circular inset at lower left shows EM view of H1
501 cell lateral elements at a synaptic invagination of S cone 15 (red arrowhead). Circular inset at
502 lower right shows a 3D view of S cone 15 (partial transparency) contacting multiple H1 cells. **D**.
503 Two H2 cells (tan and red) contacting multiple S cones, including S cone 15. Lower insets show
504 H2 cell lateral elements at S cone 15 in single layer EM view (left) and 3D (right) view
505 (conventions as in **C**).

506

507 **Figure 3. Bipolar cell types. A**. Outer stratifying types (FMB, flat midget bipolar; DB, diffuse
508 bipolar). Outer-x bipolar cells lacked a dendrite but made ribbon synapses in the IPL (Figure S6).
509 DBbroad cells extend processes across the IPL depth (Figure S7). **B.** Inner stratifying bipolar
510 types; IMB, invaginating midget bipolar; DB, diffuse bipolar types; BB, blue-cone bipolar type,
511 Inner-x bipolar (Figure S6); RB, rod bipolar. **C**. Horizontal view of spatial mosaics of axon
512 terminals for small groups of neighboring cells of each bipolar type, as indicated.

513

Figure 4. Amacrine cells. Amacrine cells in the INL (253 cells) and GCL (40 cells) were divided into 19 types (AC1-19; Table S1G). **A.** Small field, AII amacrine cells (AC2), in vertical view show outer, lobular dendrites (white arrowhead) and extensive, inner dendrites (green arrowhead). **B.** Horizontal view of the entire AII population in HFseg1; lower panel, vertical view. **C.** Starburst amacrine cells (AC7) were located primarily in the GCL (GCL, 14 cells; INL, 3 cells). White arrowheads indicate typical fasciculation of dendrites. **D.** Mosaic of starburst cells, GCL cells (red-violet) and INL cells (yellow); lower panel, vertical view. **E**. Small field amacrine type (AC11) in horizontal view with densely branched dendritic arbor. **F**. Horizontal view of the AC11 cell mosaic; lower panel, vertical view shows dendrites extend broadly across the IPL. **G.** Large field amacrine cells (AC8) with thick lobular dendrites, narrowly stratified in the outer IPL. **H.** Horizontal view of the complete mosaic; lower panel shows vertical view of outer IPL stratification. Scale bar in **C** applies to **E** and **G**. Scale bar in lower panel of **H** applies to **B, D, F**.

528 **Figure 5. Synapse detection. A**. OFF midget bipolar (yellow) and ON midget bipolar (red)
529 presynaptic to an outer-OFF (blue) and inner-ON (green) midget ganglion cell. **B.** Outgoing
530 synapses detected for the midget bipolar cell axon terminals shown in **A** (ganglion cells removed,
531 semi-transparent view). Synaptic ribbons (red/violet dots) and postsynaptic profiles were first
532 identified manually (see Figure S10; cone 22; BC 308 (IMB) and BC 303 (FMB)). Predicted
533 outgoing synapses (green dots and lines, IMB; blue dots and lines, FMB). White arrowheads
534 numbered 1-4 indicate the panels shown on the right in single layer EM view. Predicted and
535 segmented synaptic ribbons (in varied colors, red arrowheads); predicted postsynaptic segments
536 are marked by the dots and lines linking the synaptic ribbon to its postsynaptic structure
537 (unlabeled postsynaptic profiles belong to amacrine cells). Inset histogram shows precision and
538 sensitivity of ribbon detection and synaptic assignment. **C.** Inhibitory output synapses made by
539 two neighboring AII amacrine cells (purple and orange in partial transparency). Yellow dots show
540 synaptic output predictions; most synaptic outputs arise in the outer half of the IPL and are
541 presynaptic to OFF bipolar cells. Inset shows precision and sensitivity for the synapses made by
542 each AII cell. **D-E**. Single layer images showing segmented vesicle clouds (varied colors) in the
543 purple AII cell (shown in **C**) and synaptic connections predicted with an FMB cell (yellow dots
544 and lines; ribbons in the FMB are also segmented). **F-G**. Same conventions as in **D-E** but
545 showing three segmented vesicle clouds and synaptic predictions for the orange AII cell (shown
546 in **C**), with another FMB cell.

547

548 **Figure 6. Ganglion cells. A**. Cluster of inner-ON (red-violet) and outer-OFF (yellow-green)
549 midget ganglion cells; dendrites stratify broadly across inner (ON) and outer (OFF) half of the
550 IPL. **B**. Inner-ON (red-violet) and outer-OFF (yellow-green) parasol ganglion cells; dendrites
551 stratify broadly near the center of the IPL. **C**. Small bistratified ganglion cells extend dendrites
552 across the ON-OFF subdivision of the IPL. **D**. Large bistratified ganglion cells (LBGC1) show
553 large dendritic field and broad stratification coextensive with the small bistratified cells. White
554 arrowhead shows branching processes arising from the cell body of unknown significance. **E-H**,
555 Mosaic of dendritic arbors in horizontal view of the same cells shown in **A-D**. **E**. Outer-OFF
556 (yellow-green, top) and inner-ON (red-violet) midget GC. **F**. Outer-OFF parasol cell dendrites
557 show minimal overlap (inner-ON parasol mosaic not shown). **G**. Small bistratified cells show
558 minimal dendritic tree overlap. **H**. LFGC1 (Large bistratified cells) show a much larger and more
559 sparsely branching irregular tree, with greater overlap of neighboring cells. **I-K**. Morphology of
560 three additional large field types. **I**. LFGC2 (Large diffuse cells) show a densely branched tree
561 broadly stratified across the IPL. **J**. LFGC3 (Recursive bistratified cells) are narrowly bistratified
562 near center of the IPL and tend to fasciculate with starburst amacrine cells. **K**. LFGC4 (Inner
563 smooth monostratified cells) show large, monostratified dendritic trees costratified with parasol
564 cells. **L-N**. Horizontal views of the cells shown in **I-K.**

565

566

567 **Figure 7. Vertical excitatory connectome. A**. Vertical connectome for a single LM cone (cone
568 22, see details in Figure S10B). Cone pedicle and postsynaptic bipolar cells shown in silhouette.
569 Synaptic ribbons in the cone pedicle (top, OPL) and bipolar cell axon terminals (lower, IPL) are
570 shown as red balls. Inset shows all bipolar cells postsynaptic to this cone pedicle (outer, yellow-
571 gold; inner, blue-violet-red). **B**. The same views for an identified S-cone (cone 103, see details in
572 Figure S11B; synaptic ribbons, blue dots). **C**. Histogram shows output synapse numbers (left
573 axis) and percent (right axis) made via bipolar cells connected to 3 LM and 2 S cones with
574 postsynaptic GC types. Note that OFF pathway derived synapses greatly outnumber ON
575 pathway synapses. **D**. The great majority of synapses from LM and S cones are distributed to
576 midget, parasol and small bistratified ganglion cells (Major GCs) with all other large field types
577 receiving 7.9% (LM) and 6.4% (S) of the synaptic output (see also Table S2). Unidentified
578 processes account for 0.5% of total synaptic output (LM) (see Tables S2A-S2C).

579

580

STAR METHODS

Detailed methods are provided in the online version of this paper and include the following:

- KEY RESOURCES TABLE
- CONTACT FOR REAGENT AND RESOURCE SHARING
- EXPERIMENTAL MODEL AND SUBJECT DETAILS
    - Human tissue preparation and acquisition
- METHOD DETAILS
- Identification of foveal ROI, serial block-face SEM sample preparation and image acquisition
- Volume creation
    - Montaging
    - Alignment
    - Segmentation
- Synapse detection
    - Ribbon synapse detection in OPL and IPL
    - Vesicle cloud detection and inhibitory synapse assignment in the IPL
    - IPL inhibitory synapse assignment
    - Generating the cone-cone contactome
- Proofreading and synaptic connectivity and updating with the Connectome Annotation Version Engine (CAVE)

- DATA AND SOFTWARE AVAILABILITY

604 **STAR METHODS**

605

606 **KEY RESOURCES TABLE**

REAGENT or RESOURCE	SOURCE	IDENTIFIER
Biological samples		
EM human retinal samples	Medical University of Vienna	https://www.meduniwien.ac.at
Deposited data		
Electron microscopy image volume	This paper	
Segmented image data with annotated cells	This paper	
Excitatory/conventional inhibitory synaptic segmentation	This paper	
Synaptic connectivity sample tables	This paper	
CAVE	This paper	
NeuroMapsCAVE	This paper	https://neuromaps.app
Software and algorithms		
Python 3	Python.org	https://www.python.org
Jupyter Notebook 7.0.8	Jupyter.org	https://jupyter.org
Meshparty		https://github.com/CAVEconnectome/MeshParty
NeuroMaps	NeuroMaps.app	https://neuromaps.app
TrakEM2	NIH FIJI	https://fiji.sc/, RRID: SCR_002285

607

608

609 **CONTACT FOR REGENT AND RESOURCE SHARING**

610 Further information and request for resources should be directed to and will be fulfilled by the

611 Lead contact, Dennis M. Dacey (dmd@uw.edu).

612

613 **EXPERIMENTAL MODEL AND SUBJECT DETAILS**

614 **Human tissue acquisition and preparation**

615 Human eyes (52-year-old, white male; brain dead organ donor) were acquired from the Medical

616 University of Vienna, Vienna, Austria at the time of death by surgical enucleation. A small

617 incision was made to give fixative access to the posterior chamber and the retina was in this
618 way immersion fixed in 4% glutaraldehyde in 0.1 M sodium cacodylate buffer, pH7.3-7.4 at room
619 temperature. Medical history confirmed no abnormalities of the visual system recorded and no
620 driving limitations; the ocular status was defined medically as unremarkable at time of
621 enucleation. Eyes were shipped in fixative to the University of Washington where the retinas
622 were dissected and prepared for electron microscopy.

623

624 **METHOD DETAILS**

625 **Identification of foveal ROI, serial block-face SEM sample preparation and image**
626 **acquisition**

627 Retinal tissue was dissected using a light microscope to facilitate identification of the optic disc
628 and the center of the foveal pit as well as the major retinal meridians. We selected an ROI that
629 extends across absolute eccentricity of ~450-650 microns (temporal retina). This location is
630 linked to cones located ~100-300 microns from the foveal pit center due to the lateral migration
631 of retinal circuits from the cones at the foveal center. This location encompasses much of the
632 central 1 degree (~300 μm/deg) of visual angle (Figures 1A-1C).

633 The dissected retina was then plastic embedded and prepared for electron microscopy as
634 previously described[1]. In brief, the tissue was incubated in a 1.5% potassium ferrocyanide and
635 2% osmium tetroxide (OsO4) solution for 1 h. After washing, the tissue was placed in a freshly
636 made thiocarbohydrazide solution for 20 min and then rinsed and incubated in 2% OsO4 for 30
637 min. Lastly, the tissue was stained en bloc in 1% uranyl acetate overnight and subsequently
638 stained with Walton's lead aspartate, dehydrated and plastic embedded (Durcupan, 44610,
639 Sigma Aldrich). After evaluation of the ROI by semithin sectioning the tissue block was trimmed,
640 gold-coated by standard methods, and mounted in an Apreo SEM Volumescope (Thermo

641 Fisher). We cut 3028 sections at 50 nm thick for a total depth of ~150 microns, imaging an ROI
642 (180 µm tall x 180 µm wide; 5 nm pixels) that encompassed the full vertical depth of the retina,
643 from the Henle fiber layer (HFL) to the nerve fiber layer (Figure 1D). The overall ROI was
644 imaged on the blockface after each section as 25 sequential tiles (8000 x 8000 pixels or 40 x 40
645 µm; 75,700 total image tiles) with 10% overlap. Images were stitched within layer and aligned
646 across layers using standard methods available in TrakEM2 [2] (NIH image plugin; Scale Invariant
647 Feature Transform (SIFT) with affine translation) to create a good quality volume. We first
648 evaluated this TrakEM2-aligned volume by manual reconstruction of a small number of selected
649 cells and circuits [47]. To further develop this volume as a connectomic resource we applied deep-
650 learning based computational approaches to realign, segment and reconstruct all cells and
651 synaptic connections as follows [22,37].

652 **Volume creation**

653 *Montaging.* Tile offsets were determined manually, then refined by template matching at 40 nm
654 with a search window of 96 pixels. Tiles were cropped by 128 pixels to avoid edge distortions
655 and placed to minimize the sum of least squares from the new offsets. Outliers were inspected
656 and given manual placement. These cropped tiles were processed to create a pyramid of
657 encodings for resolutions between 20 nm and 640 nm [118], and then stitched to make the
658 montaged section in two steps. In the first step, only the two neighboring tiles in Y were
659 considered, with both neighbors being fixed. Using an online finetuner pyramid [118] with the
660 calculated placement as the starting point, a displacement field was generated that would warp
661 the encoded tiles to minimize the pixel difference with the fixed tiles. The encoded tiles were
662 then warped using this displacement field, eroded by a pixel to avoid partial pixels at the edge,
663 blended to the fixed tiles using the mean of the pixel values in the overlap, and then passed
664 through CLAHE enhancement to mitigate the contrast loss from the warping and blending,
665 resulting in strips of encoded tiles where every other tile had been warped. In the second step,

666 the strips of tiles from the first step were stitched to each other, holding every other strip fixed in
667 a similar process. An error map was generated at both steps by computing the difference
668 between the encodings in the overlap at 40 nm and inspected. The non-encoded tiles were
669 cropped by 394 pixels, warped according to the composed displacement fields from the
670 encodings, and combined to yield montaged sections.

671 *Alignment.* The unaligned sections were first processed to create a pyramid of encodings [118]. A
672 rigid transformation for the entire dataset was estimated using SIFT features [119] extracted from
673 the encodings at 640 nm and correspondences established between nearest and next-nearest
674 section pairs. From the rigidly aligned encodings, displacement fields at 40 nm resolution were
675 generated between nearest and next-nearest section pairs using an online finetuner pyramid [118].

676 A convolutional net trained to detect local misalignments and/or simple mismatches caused by
677 defects in the EM images was used to mask unreliable regions in each displacement field. In
678 addition, 25 sections with defects that presented with non-smooth deformations were masked
679 by hand. Pairwise displacement fields and transformation masks were then passed to a global
680 relaxation [118,120]. This relaxation was performed first at 2560 nm across all 3028 sections of the
681 dataset, and subsequently in blocks of approximately 100 sections at a resolution of 640 nm,
682 using the previously generated drift-free fields as constraints for the start and end sections of
683 each of the 31 blocks. The resulting displacement fields were composed with the earlier rigid
684 transformation and the final aligned image stack warped and rendered at 10 nm.

685 *Segmentation.* We pretrained a convolutional net to predict affinities between neighboring voxels
686 at 16×16×40 nm³ using 1,368 μm³ of manually annotated data derived from three mouse visual
687 cortex datasets [121]. We used the residual symmetric U-Net architecture [122] with modifications [123]
688 and trained with data augmentation previously described [124]. We trained the network for
689 2,000,000 iterations using four NVIDIA L4 GPUs with PyTorch data parallelism, where each GPU
690 processed individual patches with its own model replica.

691 To further fine-tune this network, we manually created training data consisting of 39 μm^3 at a
692 resolution of 20×20×50 nm^3. In contrast to the pretraining datasets, mitochondria were
693 intentionally over segmented to bias boundary detection toward a more conservative approach,
694 aiming primarily to reduce merge errors at the expense of increasing split errors. Although we
695 initially hypothesized that this mitochondrial over segmentation would minimally impact neuron
696 reconstruction accuracy, we observed that it occasionally resulted in split errors in scenarios
697 where mitochondria were tightly enclosed within very thin neuronal branches. Nevertheless, due
698 to the substantial reduction in merge errors achieved by this strategy, we considered the
699 corresponding increase in split errors acceptable. The training setup for fine-tuning was identical
700 to the pretraining configuration. We fine-tuned the network for 300,000 iterations.

701 We predicted an affinity map for the whole dataset. Dark voxels could sometimes span multiple
702 cells and cause segmentation errors. We therefore applied a binarized mask for dark voxels
703 with a threshold of 0.2, invalidating each dark voxel and its three incident affinities. The resulting
704 masked affinity map was then segmented with a mean affinity agglomeration threshold of 0.25
705 [124]. The segmentation was ingested into the Connectome Annotation Versioning Engine
706 proofreading platform, CAVE [125] for further analysis (Zetta.ai, hosting).

707 CAVE permitted proofreading to be performed by a user community accessing the web-based
708 neuroglancer interface [124,126] with dynamic updating of segment ID and related synaptic
709 connectivity. We named this segmented volume HFseg1 (Human Fovea, segmentation 1). The
710 HFseg 1 segmentation was of high initial quality such that it was possible to identify and
711 annotate all major cell classes within the volume and to sort these cells into populations of
712 distinct types using the annotation tools available in neuroglancer. Current annotations have
713 been ingested into CAVE and provide a cell type ID hypothesis that can later be tested for each
714 proposed cell population by further analysis of synaptic connectivity. All cells are accessible at
715 NeuroMaps (https://neuromaps.app).

716 Cell types were identified provisionally based on segment 3D morphology (dendritic
717 morphology, stratification depth, and spatial regularity and interaction (mosaics) and in some
718 cases nuclear morphology) with proofreading ongoing (> 25,000 edits) and applied thus far to
719 correct larger obvious mergers (primarily with glial cell processes) that interfered with cell type
720 identification and additional more detailed proofreading on circuits of interest in the current
721 survey of cone-bipolar-ganglion cell connections. The majority of cell populations were
722 unambiguously recognized based on previous studies of primate retina [62,127,128] (e.g., the S
723 cones, the H1 and H2 horizontal cells, the starburst and AII amacrine cell types, the midget,
724 diffuse and blue-cone bipolar types, or the midget, parasol and small bistratified ganglion cell
725 types); some cell types (mainly low density amacrine types) were provisionally designated
726 subject to further proofreading and connectivity analysis. The properties and relative densities of
727 these cell types provide the starting point from which the full synaptic connectome can be
728 determined after proofreading by the community, and the assignment of synaptic connections to
729 each cell in the volume. Following FlyWire[38], we have initiated an open community of retinal
730 neurobiologists (currently 7 labs participating) to use these tools to complete proofreading of the
731 HFseg1 volume.

732 **Synapse detection**

733 *Ribbon synapse detection in OPL and IPL.* A symmetric residual U-Net architecture was trained
734 on data with a resolution of 10×10×50 nm^3 using input patches of size 128×128×20 to generate
735 a probability map that indicates the likelihood of each voxel belonging to a synaptic ribbon [129].
736 To remove less robust predictions at the boundaries, only the central 96×96×16 voxels of the
737 input patch was used as the output. The model was trained on a total volume of 2,254 μm^3 of
738 manually labeled cutouts sampled from various regions across the entire dataset.

739 The ribbon segmentation was produced by (1) down sampling the probability map by 2×, (2)
740 thresholding for voxels above 0.15, and (3) using 26-connectivity to extract connected

741 components. Segments smaller than 5 voxels in a 20×20×50 nm^3 resolution were neglected to
742 eliminate spurious detections.

743 To achieve ribbon detection in the OPL segments smaller than 5 voxels in a 20×20×50 nm^3
744 resolution within the bounds of the OPL were neglected to eliminate spurious detections. For
745 each detected ribbon within a cone pedicle, postsynaptic partners were automatically identified
746 via the following steps: (1) All neighboring segments touching the pedicle within 800 nm of the
747 ribbon centroid were identified. (2) For each neighbor, a representative point close to the ribbon
748 was chosen as the postsynaptic site. These constitute the set of putative synapses for each
749 ribbon. (3) After cell identification, only putative synapses onto bipolar or horizontal cells were
750 kept; all others were filtered out (e.g. Müller glia, neighboring cones, mitochondria). (4) Finally,
751 for each distinct ribbon-postsynaptic cell pair, all but the shortest putative synapse were filtered
752 out. The result was that for each ribbon in a cone, a single synaptic connection was found onto
753 any bipolar or horizontal cell making contact with that cone pedicle within 800 nm.

754 For synaptic ribbons in the IPL segments smaller than 50 voxels in a 20×20×50 nm^3 resolution
755 within the bounds of the IPL were neglected to eliminate spurious detections. For each detected
756 ribbon, postsynaptic partners were automatically identified via the following steps: (1) Identify
757 the two largest cells within a small (500 nm) window of the centroid of the ribbon which contact
758 the presynaptic cell, and also contact each other. (2) If such a pair is found, the ribbon is
759 assumed to synapse on both (i.e., a dyadic synapse). (3) If no such pair is found, then within the
760 window, the single largest cell contacting the presynaptic cell is identified as the postsynaptic
761 partner. (4) Putative synapses were filtered by cell type, requiring the presynaptic cell to be
762 previously annotated as a bipolar cell, and the postsynaptic partner to be previously annotated
763 as amacrine, or ganglion cell. Note we did not at this time try to use a convolutional net to
764 detect a low density of possibly ribbonless synapses.

765 *Vesicle cloud detection and Inhibitory synapse assignment in the IPL.* A symmetric residual U-
766 Net architecture was trained on data with a resolution of 10×10×50 nm^3 using input patches of
767 size 128×128×20 to generate a probability map that indicates the likelihood of each voxel
768 belonging to a vesicle cloud [129]. To remove less robust predictions at the boundaries, only the
769 central 96×96×16 voxels of the input patch was used as the output. The model was trained on a
770 total volume of 2,254 μm^3 of manually labeled cutouts sampled from various regions across the
771 entire dataset (the same cutouts as ribbon synapse detection). Manual labels were roughly
772 annotated to mark approximate locations of vesicle clouds rather than precise boundaries.

773 The vesicle cloud segmentation was produced by (1) downsampling the probability map by 2×,
774 (2) thresholding for voxels above 0.15, and (3) using 26-connectivity to extract connected
775 components. Segments with fewer than 200 voxels were excluded, based on the range of
776 vesicle cloud sizes encountered.

777 *IPL inhibitory synapse assignment*. A symmetric residual U-Net architecture was trained on data
778 with a resolution of 20×20×50 nm^3 using input patches of size 24×24×8 to generate a probability
779 map that indicates the likelihood of each voxel belonging to the postsynaptic cell [129]. The model
780 was trained on 682 μm^3 of manually annotated labeled cutouts.

781 The model was applied once for each vesicle cloud detected, in a window centered on the
782 centroid of the vesicle cloud. Using the initial automatic cell segmentation, the cell with the
783 highest mean probability within the window was selected as the putative postsynaptic partner
784 [129]. Further filtering by cell type was applied, requiring the presynaptic cell to be previously
785 annotated as an amacrine cell, and the postsynaptic partner to be previously annotated as
786 amacrine, bipolar, or ganglion cell.

787 *Generating the cone-cone contactome.* The first synaptic contacts in the retina are gap junctions
788 formed among cones and between cones and rods. These junctions are harbored in large
789 dense contacts (adherens junctions) made between the photoreceptor synaptic terminals. We

790 identified this connectional relationship as follows. Cones and rods were manually identified and
791 proofread to completion. Contacts between all cones and rods in the OPL were computed using
792 abiss [130] where a contact is considered to be a set of connected voxel faces that are shared by
793 the same pair of segments. For each contact, we count the number of voxel faces along each
794 orientation (xy, xz, and yz), as well as the minimum bounding box containing all of the faces.
795 The surface area of a contact was estimated by computing the sum of the area of all faces
796 involved. Contacts were excluded from analysis if (1) the surface area of the contact was $\leq$0.04
797 μm^2 (mean surface area of contact, 0.55 ± 0.3 μm^2, n = 1141 cone-cone contacts) or (2) the
798 center of the bounding box was more than 15 μm from the approximate center of the cone
799 pedicle (manually identified). All remaining contacts were manually inspected with 1× coverage
800 to determine if they corresponded to what would be manually identified as a true cone-cone
801 contacts harboring gap junctions.

802 **Proofreading, synaptic connectivity and updating with the Connectome Annotation**
803 **Versioning Engine (CAVE)**

804 As noted above we ingested synapse predictions and cell type annotations into CAVE. A critical
805 functionality given by CAVE is that is allows collaborative users to programmatically query the
806 up-to-date proofread connectivity graph (synaptic connectivity is updated during proofreading of
807 each segment-cell type) as well as any changes made to the metadata (cell type IDs,
808 descriptions, or other annotations). We used the Jupyter notebook application to execute
809 Python code that queried the HFseg1 dataset by leveraging Python libraries that interact with
810 the human foveal dataset, enabling access to segment IDs and synaptic assignments.

811

812 **DATA AND SOFTWARE AVAILABILITY**

The HFseg1 dataset (volume, segmentation, synaptic detection and full annotation) are currently hosted by Zetta.ai (https://zetta.ai/) and all data is accessible by permission. The latest version of the HFseg1 dataset is also available at NeuroMaps (https://neuromaps.app).

818 **References**

819 1. Ramon y Cajal, S. (1892). La rètine des vertèbrès. La Cellule *9*, 119-257.

820 2. Masland, R.H., and Raviola, E. (2000). Confronting complexity: strategies for
821 understanding the microcircuitry of the retina. Annual review of neuroscience *23*, 249-
822 284.

823 3. Rodieck, R.W. (1973). The vertebrate retina: Principles of structure and function (W.H.
824 Freeman).

825 4. Helmstaedter, M., Briggman, K.L., Turaga, S.C., Jain, V., Seung, H.S., and Denk, W.
826 (2013). Connectomic reconstruction of the inner plexiform layer in the mouse retina.
827 Nature *500*, 168-174. 10.1038/nature12346.

828 5. Kim, J.S., Greene, M.J., Zlateski, A., Lee, K., Richardson, M., Turaga, S.C., Purcaro, M.,
829 Balkam, M., Robinson, A., Behabadi, B.F., et al. (2014). Space-time wiring specificity
830 supports direction selectivity in the retina. Nature *509*, 331-336. 10.1038/nature13240.

831 6. Briggman, K.L., Helmstaedter, M., and Denk, W. (2011). Wiring specificity in the
832 direction-selectivity circuit of the retina. Nature *471*, 183-188. 10.1038/nature09818.

833 7. Anderson, J.R., Jones, B.W., Watt, C.B., Shaw, M.V., Yang, J.H., Demill, D., Lauritzen,
834 J.S., Lin, Y., Rapp, K.D., Mastronarde, D., et al. (2011). Exploring the retinal
835 connectome. Molecular vision *17*, 355-379.

836 8. Calkins, D.J., Schein, S.J., Tsukamoto, Y., and Sterling, P. (1994). M and L cones in
837 macaque fovea connect to midget ganglion cells by different numbers of excitatory
838 synapses. Nature *371*, 70-72.

839 9. Calkins, D.J., and Sterling, P. (1996). Absence of spectrally specific lateral inputs to
840 midget ganglion cells in primate retina. Nature *381*, 613-615.

841 10. Shekhar, K., Lapan, S.W., Whitney, I.E., Tran, N.M., Macosko, E.Z., Kowalczyk, M.,
842 Adiconis, X., Levin, J.Z., Nemesh, J., Goldman, M., et al. (2016). Comprehensive
843 Classification of Retinal Bipolar Neurons by Single-Cell Transcriptomics. Cell *166*, 1308-
844 1323 e1330. 10.1016/j.cell.2016.07.054.

845 11. Peng, Y.R., Shekhar, K., Yan, W., Herrmann, D., Sappington, A., Bryman, G.S., van Zyl,
846 T., Do, M.T.H., Regev, A., and Sanes, J.R. (2019). Molecular Classification and
847 Comparative Taxonomics of Foveal and Peripheral Cells in Primate Retina. Cell *176*,
848 1222-1237. 10.1016/j.cell.2019.01.004.

849 12. Yan, W., Peng, Y.R., van Zyl, T., Regev, A., Shekhar, K., Juric, D., and Sanes, J.R.
850 (2020). Cell Atlas of The Human Fovea and Peripheral Retina. Sci Rep *10*, 9802.
851 10.1038/s41598-020-66092-9.

852 13. Hahn, J., Monavarfeshani, A., Qiao, M., Kao, A.H., Kolsch, Y., Kumar, A., Kunze, V.P.,
853 Rasys, A.M., Richardson, R., Wekselblatt, J.B., et al. (2023). Evolution of neuronal cell
854 classes and types in the vertebrate retina. Nature *624*, 415-424. 10.1038/s41586-023-
855 06638-9.

14. Li, J., Wang, J., Ibarra, I.L., Cheng, X., Luecken, M.D., Lu, J., Monavarfeshani, A., Yan, W., Zheng, Y., Zuo, Z., et al. (2023). Integrated multi-omics single cell atlas of the human retina. Res Sq. 10.21203/rs.3.rs-3471275/v1.

15. Dorkenwald, S., Matsliah, A., Sterling, A.R., Schlegel, P., Yu, S.C., McKellar, C.E., Lin, A., Costa, M., Eichler, K., Yin, Y., et al. (2024). Neuronal wiring diagram of an adult brain. Nature *634*, 124-138. 10.1038/s41586-024-07558-y.

16. Azevedo, A., Lesser, E., Phelps, J.S., Mark, B., Elabbady, L., Kuroda, S., Sustar, A., Moussa, A., Khandelwal, A., Dallmann, C.J., et al. (2024). Connectomic reconstruction of a female Drosophila ventral nerve cord. Nature *631*, 360-368. 10.1038/s41586-024-07389-x.

17. Abbott, L.F., Bock, D.D., Callaway, E.M., Denk, W., Dulac, C., Fairhall, A.L., Fiete, I., Harris, K.M., Helmstaedter, M., Jain, V., et al. (2020). The Mind of a Mouse. Cell *182*, 1372-1376. 10.1016/j.cell.2020.08.010.

18. Shapson-Coe, A., Januszewski, M., Berger, D.R., Pope, A., Wu, Y., Blakely, T., Schalek, R.L., Li, P.H., Wang, S., Maitin-Shepard, J., et al. (2024). A petavoxel fragment of human cerebral cortex reconstructed at nanoscale resolution. Science *384*, eadk4858. 10.1126/science.adk4858.

19. Loomba, S., Straehle, J., Gangadharan, V., Heike, N., Khalifa, A., Motta, A., Ju, N., Sievers, M., Gempt, J., Meyer, H.S., and Helmstaedter, M. (2022). Connectomic comparison of mouse and human cortex. Science *377*, eabo0924. 10.1126/science.abo0924.

20. Lichtman, J.W., and Sanes, J.R. (2008). Ome sweet ome: what can the genome tell us about the connectome? Current opinion in neurobiology *18*, 346-353. 10.1016/j.conb.2008.08.010.

21. Ding, Z., Fahey, P.G., Papadopoulos, S., Wang, E.Y., Celii, B., Papadopoulos, C., Kunin, A.B., Chang, A., Fu, J., Ding, Z., et al. (2023). Functional connectomics reveals general wiring rule in mouse visual cortex. bioRxiv. 10.1101/2023.03.13.531369.

22. Turner, N.L., Macrina, T., Bae, J.A., Yang, R., Wilson, A.M., Schneider-Mizell, C., Lee, K., Lu, R., Wu, J., Bodor, A.L., et al. (2022). Reconstruction of neocortex: Organelles, compartments, cells, circuits, and activity. Cell *185*, 1082-1100 e1024. 10.1016/j.cell.2022.01.023.

23. Wandell, B.A., Dumoulin, S.O., and Brewer, A.A. (2007). Visual field maps in human cortex. Neuron *56*, 366-383. 10.1016/j.neuron.2007.10.012.

24. Sereno, M.I., Sood, M.R., and Huang, R.S. (2022). Topological Maps and Brain Computations From Low to High. Frontiers in systems neuroscience *16*, 787737. 10.3389/fnsys.2022.787737.

25. Harvey, B.M., and Dumoulin, S.O. (2011). The relationship between cortical magnification factor and population receptive field size in human visual cortex: constancies in cortical architecture. J Neurosci *31*, 13604-13612. 10.1523/JNEUROSCI.2572-11.2011.

896 26. Sereno, M.I., Dale, A.M., Reppas, J.B., Kwong, K.K., Belliveau, J.W., Brady, T.J., Rosen,
897 B.R., and Tootell, R.B. (1995). Borders of multiple visual areas in humans revealed by
898 functional magnetic resonance imaging. Science *268*, 889-893.
899 10.1126/science.7754376.

900 27. Schira, M.M., Tyler, C.W., Breakspear, M., and Spehar, B. (2009). The foveal confluence
901 in human visual cortex. J Neurosci *29*, 9050-9058. 10.1523/JNEUROSCI.1760-09.2009.

902 28. Baden, T., Berens, P., Franke, K., Roman Roson, M., Bethge, M., and Euler, T. (2016).
903 The functional diversity of retinal ganglion cells in the mouse. Nature *529*, 345-350.
904 10.1038/nature16468.

905 29. Bae, J.A., Mu, S., Kim, J.S., Turner, N.L., Tartavull, I., Kemnitz, N., Jordan, C.S., Norton,
906 A.D., Silversmith, W.M., Prentki, R., et al. (2018). Digital Museum of Retinal Ganglion
907 Cells with Dense Anatomy and Physiology. Cell *173*, 1293-1306 e1219.
908 10.1016/j.cell.2018.04.040.

909 30. Goetz, J., Jessen, Z.F., Jacobi, A., Mani, A., Cooler, S., Greer, D., Kadri, S., Segal, J.,
910 Shekhar, K., Sanes, J.R., and Schwartz, G.W. (2022). Unified classification of mouse
911 retinal ganglion cells using function, morphology, and gene expression. Cell reports *40*,
912 111040. 10.1016/j.celrep.2022.111040.

913 31. Masri, R.A., Percival, K.A., Koizumi, A., Martin, P.R., and Grunert, U. (2019). Survey of
914 retinal ganglion cell morphology in marmoset. J Comp Neurol *527*, 236-258.
915 10.1002/cne.24157.

32. Kim, Y.J., Peterson, B.B., Crook, J.D., Joo, H.R., Wu, J., Puller, C., Robinson, F.R., Gamlin, P.D., Yau, K.W., Viana, F., et al. (2022). Origins of direction selectivity in the primate retina. Nature communications *13*, 2862. 10.1038/s41467-022-30405-5.

33. Curcio, C.A., Sloan, K.R., Kalina, R.E., and Hendrickson, A.E. (1990). Human photoreceptor topography. J.Comp.Neurol. *292*, 497-523.

34. Curcio, C.A., Kar, D., Owsley, C., Sloan, K.R., and Ach, T. (2024). Age-Related Macular Degeneration, a Mathematically Tractable Disease. Investigative ophthalmology & visual science *65*, 4. 10.1167/iovs.65.3.4.

35. Schein, S.J. (1988). Anatomy of macaque fovea and spatial densities of neurons in foveal representation. J Comp Neurol *269*, 479-505. 10.1002/cne.902690403 [doi].

36. Drasdo, N., Millican, C.L., Katholi, C.R., and Curcio, C.A. (2007). The length of Henle fibers in the human retina and a model of ganglion receptive field density in the visual field. Vision Res *47*, 2901-2911. 10.1016/j.visres.2007.01.007.

37. Lee, K., Turner, N., Macrina, T., Wu, J., Lu, R., and Seung, H.S. (2019). Convolutional nets for reconstructing neural circuits from brain images acquired by serial section electron microscopy. Current opinion in neurobiology *55*, 188-198. 10.1016/j.conb.2019.04.001.

38. Dorkenwald, S., McKellar, C.E., Macrina, T., Kemnitz, N., Lee, K., Lu, R., Wu, J., Popovych, S., Mitchell, E., Nehoran, B., et al. (2022). FlyWire: online community for whole-brain connectomics. Nature methods *19*, 119-128. 10.1038/s41592-021-01330-0.

936 39. Masri, R.A., Greferath, U., Fletcher, E.L., Martin, P.R., and Grünert, U. (2025).
937 Immunohistochemistry and spatial density of Müller cells in the human fovea.
938 Investigative ophthalmology & visual science *in press*.

939 40. Singaravelu, J., Zhao, L., Fariss, R.N., Nork, T.M., and Wong, W.T. (2017). Microglia in
940 the primate macula: specializations in microglial distribution and morphology with retinal
941 position and with aging. Brain Struct Funct *222*, 2759-2771. 10.1007/s00429-017-1370-
942 x.

943 41. Goyal, M., Bordt, A.S., Neitz, J., and Marshak, D.W. (2023). Trogocytosis of neurons and
944 glial cells by microglia in a healthy adult macaque retina. Sci Rep *13*, 633.
945 10.1038/s41598-023-27453-2.

946 42. Lee, S.C.S., Martin, P.R., and Grunert, U. (2019). Topography of Neurons in the Rod
947 Pathway of Human Retina. Investigative ophthalmology & visual science *60*, 2848-2859.
948 10.1167/iovs.19-27217.

949 43. Kim, Y.J., Packer, O., Pollreisz, A., Martin, P.R., Grunert, U., and Dacey, D.M. (2023).
950 Comparative connectomics reveals noncanonical wiring for color vision in human foveal
951 retina. Proceedings of the National Academy of Sciences of the United States of America
952 *120*, e2300545120. 10.1073/pnas.2300545120.

953 44. O'Brien, J.J., Chen, X., Macleish, P.R., O'Brien, J., and Massey, S.C. (2012).
954 Photoreceptor coupling mediated by connexin36 in the primate retina. J Neurosci *32*,
955 4675-4687. 10.1523/JNEUROSCI.4749-11.2012.

956 45. Hornstein, E.P., Verweij, J., and Schnapf, J.L. (2004). Electrical coupling between red
957 and green cones in primate retina. Nature neuroscience *7*, 745-750.

958 46. Li, W., and DeVries, S.H. (2004). Separate blue and green cone networks in the
959 mammalian retina. Nature neuroscience *7*, 751-756.

960 47. Kim, Y.J., Packer, O., and Dacey, D.M. (2024). A circuit motif for color in the human
961 foveal retina. Proceedings of the National Academy of Sciences of the United States of
962 America *121*, e2405138121. 10.1073/pnas.2405138121.

963 48. Kolb, H., Goede, P., Roberts, S., McDermott, R., and Gouras, P. (1997). Uniqueness of
964 the S-cone pedicle in the human retina and consequences for color processing.
965 J.Comp.Neurol. *386*, 443-460.

966 49. Tsukamoto, Y., Masarachia, P., Schein, S.J., and Sterling, P. (1992). Gap junctions
967 between the pedicles of macaque foveal cones. Vision Res. *32*, 1809-1815.

968 50. Martin, P.R., Blessing, E.M., Buzas, P., Szmajda, B.A., and Forte, J.D. (2011).
969 Transmission of colour and acuity signals by parvocellular cells in marmoset monkeys. J
970 Physiol *589*, 2795-2812. 10.1113/jphysiol.2010.194076.

971 51. Wool, L.E., Crook, J.D., Troy, J.B., Packer, O.S., Zaidi, Q., and Dacey, D.M. (2018).
972 Nonselective Wiring Accounts for Red-Green Opponency in Midget Ganglion Cells of the
973 Primate Retina. J Neurosci *38*, 1520-1540. 10.1523/JNEUROSCI.1688-17.2017.

52. Crook, J.D., Manookin, M.B., Packer, O.S., and Dacey, D.M. (2011). Horizontal cell feedback without cone type-selective inhibition mediates "red-green" color opponency in midget ganglion cells of the primate retina. J Neurosci *31*, 1762-1772. 10.1523/JNEUROSCI.4385-10.2011.

53. Dacey, D.M., Lee, B.B., Stafford, D.K., Pokorny, J., and Smith, V.C. (1996). Horizontal cells of the primate retina: cone specificity without spectral opponency. Science *271*, 656-659.

54. Kolb, H., Mariani, A., and Gallego, A. (1980). A second type of horizontal cell in the monkey retina. J.Comp.Neurol. *189*, 31-44.

55. Goodchild, A.K., Chan, T.L., and Grünert, U. (1996). Horizontal cell connections with short-wavelength-sensitive cones in macaque monkey retina. Vis. Neurosci. *13*, 833-845.

56. Ahnelt, P., and Kolb, H. (1994). Horizontal cells and cone photoreceptors in human retina: A golgi-electron microscopic study of spectral connectivity. J.Comp.Neurol. *343*, 406-427.

57. Dacey, D.M., Lee, B.B., Stafford, D.K., Pokorny, J., and Smith, V.C. (1996). Horizontal cells of the primate retina: cone specificity without spectral opponency. Science *271*, 656-659. 10.1126/science.271.5249.656.

992 58. Masri, R.A., Weltzien, F., Purushothuman, S., Lee, S.C.S., Martin, P.R., and Grunert, U.
993 (2021). Composition of the Inner Nuclear Layer in Human Retina. Investigative
994 ophthalmology & visual science *62*, 22. 10.1167/iovs.62.9.22.

995 59. Peichl, L., Sandmann, D., and Boycott, B.B. (1998). Comparative anatomy and function
996 of mammalian horizontal cells. In Development and Organization of the Retina, Chalupa,
997 and Finlay, eds. (Plenum Press), pp. 147-172.

998 60. Dacheux, R.F., and Raviola, E. (1990). Physiology of HI horizontal cells in the primate
999 retina. Proc.R.Soc.Lond.B Biol.Sci. *239*, 213-230.

1000 61. Chan, T.L., and Grünert, U. (1998). Horizontal cell connections with short wavelength-
1001 sensitive cones in the retina: A comparison between New World and Old World
1002 primates. J.Comp.Neurol. *393*, 196-209.

1003 62. Grunert, U., and Martin, P.R. (2020). Cell types and cell circuits in human and non-
1004 human primate retina. Progress in retinal and eye research, 100844.
1005 10.1016/j.preteyeres.2020.100844.

1006 63. Puthussery, T., Gayet-Primo, J., Taylor, W.R., and Haverkamp, S. (2011).
1007 Immunohistochemical identification and synaptic inputs to the diffuse bipolar cell type
1008 DB1 in macaque retina. J Comp Neurol *519*, 3640-3656. 10.1002/cne.22756.

1009 64. Puthussery, T., Percival, K.A., Venkataramani, S., Gayet-Primo, J., Grunert, U., and
1010 Taylor, W.R. (2014). Kainate receptors mediate synaptic input to transient and sustained

1011 OFF visual pathways in primate retina. J Neurosci *34*, 7611-7621.
1012 10.1523/JNEUROSCI.4855-13.2014.

1013 65. Puthussery, T., Venkataramani, S., Gayet-Primo, J., Smith, R.G., and Taylor, W.R.
1014 (2013). NaV1.1 channels in axon initial segments of bipolar cells augment input to
1015 magnocellular visual pathways in the primate retina. J Neurosci *33*, 16045-16059.
1016 10.1523/JNEUROSCI.1249-13.2013.

1017 66. Tsukamoto, Y., and Omi, N. (2015). OFF bipolar cells in macaque retina: type-specific
1018 connectivity in the outer and inner synaptic layers. Frontiers in neuroanatomy *9*, 122.
1019 10.3389/fnana.2015.00122.

1020 67. Tsukamoto, Y., and Omi, N. (2014). Some OFF bipolar cell types make contact with both
1021 rods and cones in macaque and mouse retinas. Frontiers in neuroanatomy *8*, 105.
1022 10.3389/fnana.2014.00105.

1023 68. Haverkamp, S., Haeseleer, F., and Hendrickson, A. (2003). A comparison of
1024 immunocytochemical markers to identify bipolar cell types in human and monkey retina.
1025 Visual neuroscience *20*, 589-600.

1026 69. Masri, R.A., Grunert, U., and Martin, P.R. (2020). Analysis of Parvocellular and
1027 Magnocellular Visual Pathways in Human Retina. J Neurosci *40*, 8132-8148.
1028 10.1523/JNEUROSCI.1671-20.2020.

1029 70. Grünert, U., Martin, P.R., and Wässle, H. (1994). Immunocytochemical analysis of
1030 bipolar cells in the macaque monkey retina. J.Comp.Neurol. *348*, 607-627.

1031 71. Weltzien, F., Percival, K.A., Martin, P.R., and Grunert, U. (2015). Analysis of bipolar and
1032 amacrine populations in marmoset retina. J Comp Neurol *523*, 313-334.
1033 10.1002/cne.23683.

1034 72. Tsukamoto, Y., and Omi, N. (2016). ON Bipolar Cells in Macaque Retina: Type-Specific
1035 Synaptic Connectivity with Special Reference to OFF Counterparts. Frontiers in
1036 neuroanatomy *10*, 104. 10.3389/fnana.2016.00104.

1037 73. Joo, H.R., Peterson, B.B., Haun, T.J., and Dacey, D.M. (2011). Characterization of a
1038 novel large-field cone bipolar cell type in the primate retina: evidence for selective cone
1039 connections. Visual neuroscience *28*, 29-37. 10.1017/S0952523810000374.

1040 74. Tsukamoto, Y., and Omi, N. (2022). Multiple Invagination Patterns and Synaptic Efficacy
1041 in Primate and Mouse Rod Synaptic Terminals. Investigative ophthalmology & visual
1042 science *63*, 11. 10.1167/iovs.63.8.11.

1043 75. Saha, A., Zuniga, J., Mian, K., Zhai, H., Derr, P.J., Hoon, M., and Sinha, R. (2023).
1044 Regional variation in the organization and connectivity of the first synapse in the primate
1045 night vision pathway. iScience *26*, 108113. 10.1016/j.isci.2023.108113.

1046 76. Grünert, U., and Martin, P.R. (1991). Rod bipolar cells in the macaque monkey retina:
1047 Immunoreactivity and connectivity. J.Neurosci. *11*, 2742-2758.

1048 77. Kolb, H., Zhang, L., and Dekorver, L. (1993). Differential staining of neurons in the
1049 human retina with antibodies to protein kinase C isozymes. Vis.Neurosci. *10*, 341-351.

1050 78. Della Santina, L., Kuo, S.P., Yoshimatsu, T., Okawa, H., Suzuki, S.C., Hoon, M.,
1051 Tsuboyama, K., Rieke, F., and Wong, R.O.L. (2016). Glutamatergic Monopolar
1052 Interneurons Provide a Novel Pathway of Excitation in the Mouse Retina. Current
1053 biology : CB *26*, 2070-2077. 10.1016/j.cub.2016.06.016.

1054 79. Calkins, D.J., Tsukamoto, Y., and Sterling, P. (1996). Foveal cones form basal as well as
1055 invaginating junctions with diffuse ON bipolar cells. Vision Res. *36*, 3373-3381.

1056 80. Strettoi, E., Raviola, E., and Dacheux, R.F. (1992). Synaptic connections of the narrow-
1057 field, bistratified rod amacrine cell (AII) in the rabbit retina. J.Comp.Neurol. *325*, 152-168.

1058 81. Strettoi, E., Masri, R.A., and Grunert, U. (2018). AII amacrine cells in the primate fovea
1059 contribute to photopic vision. Sci Rep *8*, 16429. 10.1038/s41598-018-34621-2.

1060 82. Lee, S.C., Weltzien, F., Madigan, M.C., Martin, P.R., and Grunert, U. (2016).
1061 Identification of AII amacrine, displaced amacrine, and bistratified ganglion cell types in
1062 human retina with antibodies against calretinin. J Comp Neurol *524*, 39-53.
1063 10.1002/cne.23821.

1064 83. Demb, J.B., and Singer, J.H. (2012). Intrinsic properties and functional circuitry of the AII
1065 amacrine cell. Visual neuroscience *29*, 51-60. 10.1017/S0952523811000368.

1066 84. Vaney, D.I., Sivyer, B., and Taylor, W.R. (2012). Direction selectivity in the retina:
1067 symmetry and asymmetry in structure and function. Nature reviews. Neuroscience *13*,
1068 194-208. 10.1038/nrn3165.

1069 85. Rodieck, R.W., and Marshak, D.W. (1992). Spatial density and distribution of choline
1070 acetyltransferase immunoreactive cells in human, macaque, and baboon retinas.
1071 J.Comp.Neurol. *321*, 46-64.

1072 86. Rodieck, R.W. (1989). Starburst amacrine cells of the primate retina. J.Comp.Neurol.
1073 *285*, 18-37.

1074 87. Zhang, C., Yu, W.Q., Hoshino, A., Huang, J., Rieke, F., Reh, T.A., and Wong, R.O.L.
1075 (2019). Development of ON and OFF cholinergic amacrine cells in the human fetal
1076 retina. J Comp Neurol *527*, 174-186. 10.1002/cne.24405.

1077 88. Polyak, S.L. (1941). The Retina (University of Chicago Press).

1078 89. Mariani, A.P. (1990). Amacrine cells of the rhesus monkey retina. J.Comp.Neurol. *301*,
1079 382-400.

1080 90. Boycott, B.B., and Dowling, J.E. (1969). Organization of the primate retina: light
1081 microscopy. Philos.Trans.R.Soc.Lond.B Biol.Sci. *255*, 109-184.

1082 91. Klump, K.E., Zhang, A.J., Wu, S.M., and Marshak, D.W. (2009). Parvalbumin-
1083 immunoreactive amacrine cells of macaque retina. Visual neuroscience *26*, 287-296.
1084 10.1017/S0952523809090075.

1085 92. Haverkamp, S., Grunert, U., and Wassle, H. (2000). The cone pedicle, a complex
1086 synapse in the retina. Neuron *27*, 85-95. 10.1016/s0896-6273(00)00011-8.

1087 93. Grabner, C.P., Futagi, D., Shi, J., Bindokas, V., Kitano, K., Schwartz, E.A., and DeVries,
1088 S.H. (2023). Mechanisms of simultaneous linear and nonlinear computations at the
1089 mammalian cone photoreceptor synapse. Nature communications *14*, 3486.
1090 10.1038/s41467-023-38943-2.

1091 94. Herr, S., Ngo, I.T., Huang, T.M., Klug, K., Sterling, P., and Schein, S. (2011). Cone
1092 synapses in macaque fovea: II. Dendrites of OFF midget bipolar cells exhibit Inner
1093 Densities similar to their Outer synaptic Densities in basal contacts with cone terminals.
1094 Visual neuroscience *28*, 17-28. 10.1017/S0952523810000465.

1095 95. Wässle, H., Grünert, U., Chun, M.H., and Boycott, B.B. (1995). The rod pathway of the
1096 macaque monkey retina: Identification of AII-amacrine cells with antibodies against
1097 calretinin. J.Comp.Neurol. *361*, 537-551.

1098 96. Grünert, U. (1997). Anatomical evidence for rod input to the parvocellular pathway in the
1099 visual system of the primate. Eur.J.Neurosci. *9*, 617-621.

1100 97. Dacey, D.M. (1993). The mosaic of midget ganglion cells in the human retina.
1101 J.Neurosci. *13*, 5334-5355.

1102 98. Calkins, D.J., Tsukamoto, Y., and Sterling, P. (1998). Microcircuitry and mosaic of a blue-
1103 yellow ganglion cell in the primate retina. J.Neurosci. *18*, 3373-3385.

1104 99. Dacey, D.M., Peterson, B.B., Robinson, F.R., and Gamlin, P.D. (2003). Fireworks in the
1105 primate retina: in vitro photodynamics reveals diverse LGN-projecting ganglion cell
1106 types. Neuron *37*, 15-27.

1107 100. Peterson, B.B., and Dacey, D.M. (2000). Morphology of wide-field bistratified and diffuse
1108 human retinal ganglion cells. Visual neuroscience *17*, 567-578.

1109 101. Crook, J.D., Peterson, B.B., Packer, O.S., Robinson, F.R., Gamlin, P.D., Troy, J.B., and
1110 Dacey, D.M. (2008). The smooth monostratified ganglion cell: evidence for spatial
1111 diversity in the Y-cell pathway to the lateral geniculate nucleus and superior colliculus in
1112 the macaque monkey. J Neurosci *28*, 12654-12671. 10.1523/JNEUROSCI.2986-
1113 08.2008.

1114 102. Liao, H.W., Ren, X., Peterson, B.B., Marshak, D.W., Yau, K.W., Gamlin, P.D., and Dacey,
1115 D.M. (2016). Melanopsin-expressing ganglion cells on macaque and human retinas form
1116 two morphologically distinct populations. J Comp Neurol *524*, 2845-2872.
1117 10.1002/cne.23995.

1118 103. Wassle, H., Puller, C., Muller, F., and Haverkamp, S. (2009). Cone contacts, mosaics,
1119 and territories of bipolar cells in the mouse retina. J Neurosci *29*, 106-117.
1120 29/1/106[pii]10.1523JNEUROSCI.4442-08.2009 [doi].

1121 104. Ratliff, C.P., Borghuis, B.G., Kao, Y.H., Sterling, P., and Balasubramanian, V. (2010).
1122 Retina is structured to process an excess of darkness in natural scenes. Proceedings of
1123 the National Academy of Sciences of the United States of America *107*, 17368-17373.
1124 10.1073/pnas.1005846107.

1125 105. Komban, S.J., Alonso, J.M., and Zaidi, Q. (2011). Darks are processed faster than lights.
1126 J Neurosci *31*, 8654-8658. 10.1523/JNEUROSCI.0504-11.2011.

1127 106. Rahimi-Nasrabadi, H., Moore-Stoll, V., Tan, J., Dellostritto, S., Jin, J., Dul, M.W., and
1128 Alonso, J.M. (2023). Luminance Contrast Shifts Dominance Balance between ON and
1129 OFF Pathways in Human Vision. J Neurosci *43*, 993-1007. 10.1523/JNEUROSCI.1672-
1130 22.2022.

1131 107. Jin, J., Wang, Y., Lashgari, R., Swadlow, H.A., and Alonso, J.M. (2011). Faster
1132 thalamocortical processing for dark than light visual targets. J Neurosci *31*, 17471-
1133 17479. 10.1523/JNEUROSCI.2456-11.2011.

1134 108. Jin, J., Wang, Y., Swadlow, H.A., and Alonso, J.M. (2011). Population receptive fields of
1135 ON and OFF thalamic inputs to an orientation column in visual cortex. Nature
1136 neuroscience *14*, 232-238. 10.1038/nn.2729.

1137 109. Nern, A., Loesche, F., Takemura, S.Y., Burnett, L.E., Dreher, M., Gruntman, E., Hoeller,
1138 J., Huang, G.B., Januszewski, M., Klapoetke, N.C., et al. (2025). Connectome-driven
1139 neural inventory of a complete visual system. Nature. 10.1038/s41586-025-08746-0.

1140 110. Zhang, L., Cavallini, M., Wang, J., Xin, R., Zhang, Q., Feng, G., Sanes, J.R., and Peng,
1141 Y.R. (2024). Evolutionary and developmental specialization of foveal cell types in the
1142 marmoset. Proceedings of the National Academy of Sciences of the United States of
1143 America *121*, e2313820121. 10.1073/pnas.2313820121.

1144 111. Cowan, C.S., Renner, M., De Gennaro, M., Gross-Scherf, B., Goldblum, D., Hou, Y.,
1145 Munz, M., Rodrigues, T.M., Krol, J., Szikra, T., et al. (2020). Cell Types of the Human
1146 Retina and Its Organoids at Single-Cell Resolution. Cell *182*, 1623-1640 e1634.
1147 10.1016/j.cell.2020.08.013.

1148 112. Wang, A.Y.M., Kulkarni, M.M., McLaughlin, A.J., Gayet, J., Smith, B.E., Hauptschein, M.,
1149 McHugh, C.F., Yao, Y.Y., and Puthussery, T. (2023). An ON-type direction-selective
1150 ganglion cell in primate retina. Nature *623*, 381-386. 10.1038/s41586-023-06659-4.

1151 113. Shevell, S.K., and Martin, P.R. (2017). Color opponency: tutorial. Journal of the Optical
1152 Society of America. A, Optics, image science, and vision *34*, 1099-1108.
1153 10.1364/JOSAA.34.001099.

1154 114. Stockman, A., and Brainard, D.H. (2010). Color Vision Mechanisms. In OSA Handbook
1155 of Optics, M. Bass, ed. (McGraw-Hill), pp. 11.11-11.104.

1156 115. Hsu, A., Smith, R.G., Buchsbaum, G., and Sterling, P. (2000). Cost of cone coupling to
1157 trichromacy in primate fovea. Journal of the Optical Society of America. A, Optics, image
1158 science, and vision *17*, 635-640.

1159 116. DeVries, S.H., Qi, X., Smith, R., Makous, W., and Sterling, P. (2002). Electrical coupling
1160 between mammalian cones. Current biology : CB *12*, 1900-1907.

1161 117. Schlegel, P., Yin, Y., Bates, A.S., Dorkenwald, S., Eichler, K., Brooks, P., Han, D.S.,
1162 Gkantia, M., Dos Santos, M., Munnelly, E.J., et al. (2024). Whole-brain annotation and
1163 multi-connectome cell typing of Drosophila. Nature *634*, 139-152. 10.1038/s41586-024-
1164 07686-5.

1165 118. Popovych, S., Macrina, T., Kemnitz, N., Castro, M., Nehoran, B., Jia, Z., Bae, J.A.,
1166 Mitchell, E., Mu, S., Trautman, E.T., et al. (2024). Petascale pipeline for precise

alignment of images from serial section electron microscopy. Nature communications *15*, 289. 10.1038/s41467-023-44354-0.

119. Lowe, D.G. (1999). Object recognition from local scale-invariant features. Proceedings of the Seventh IEEE International Conference on Computer Vision. IEEE.

120. Saalfeld, S., Fetter, R., Cardona, A., and Tomancak, P. (2012). Elastic volume reconstruction from series of ultra-thin microscopy sections. Nature methods *9*, 717-720. 10.1038/nmeth.2072.

121. Consortium, T.M., Bae, J.A., Baptiste, M., Bishop, C.A., Bodor, A.L., Brittain, D., Buchanan, J., Bumbarger, D.J., Castro, M.A., Celii, B., et al. (2023). Functional connectomics spanning multiple areas of mouse visual cortex. bioRxiv, 2021.2007.2028.454025. 10.1101/2021.07.28.454025.

122. Lee, K., Zung, J., Li, P.H., Jain, V., and Seung, H.S. (2017). Superhuman accuracy on the SNEMI3D connectomics challenge. arXiv *preprint arXiv:1706.00120*.

123. Lee, K., Lu, R., Luther, K., and Seung, H.S. (2021). Learning and Segmenting Dense Voxel Embeddings for 3D Neuron Reconstruction. IEEE Trans Med Imaging *40*, 3801-3811. 10.1109/TMI.2021.3097826.

124. Macrina, T., Lee, K., Lu, R., Turner, N.L., Wu, J., Popovych, S., Silversmith, W., Kemnitz, N., Bae, J.A., Castro, M.A., et al. (2021). Petascale neural circuit reconstruction: automated methods. bioRxiv, 2021.2008.2004.455162. 10.1101/2021.08.04.455162.

125. Dorkenwald, S., Schneider-Mizell, C.M., Brittain, D., Halageri, A., Jordan, C., Kemnitz, N., Castro, M.A., Silversmith, W., Maitin-Shephard, J., Troidl, J., et al. (2023). CAVE: Connectome Annotation Versioning Engine. bioRxiv. 10.1101/2023.07.26.550598.

126. Maitin-Shepard, J., Baden, A., Silversmith, W., Perlman, E., Collman, F., Blakely, T., Funke, J., Jordan, C., Falk, B., Kemnitz, N., et al. (2021). google/neuroglancer.

127. Boycott, B.B., and Wässle, H. (1991). Morphological classification of bipolar cells of the primate retina. Eur.J.Neurosci. *3*, 1069-1088.

128. Wässle, H., and Boycott, B.B. (1991). Functional architecture of the mammalian retina. Physiol.Rev. *71*, 447-480.

129. Turner, N.L., Lee, K., Lu, R., Wu, J., Ih, D., and Seung, H.S. (2020). Synaptic Partner Assignment Using Attentional Voxel Association Networks. pp. 1-5.

130. Lu, R., Zlateski, A., and Seung, H.S. (2021). Large-scale image segmentation based on distributed clustering algorithms. arXiv *arXiv. http://arxiv.org/abs/2106.10795 [cs.CV]*, 1-8. https://doi.org/10.48550/arXiv.2106.10795.

1201 **Figures (Figure 1 to Figure 7)**

1202

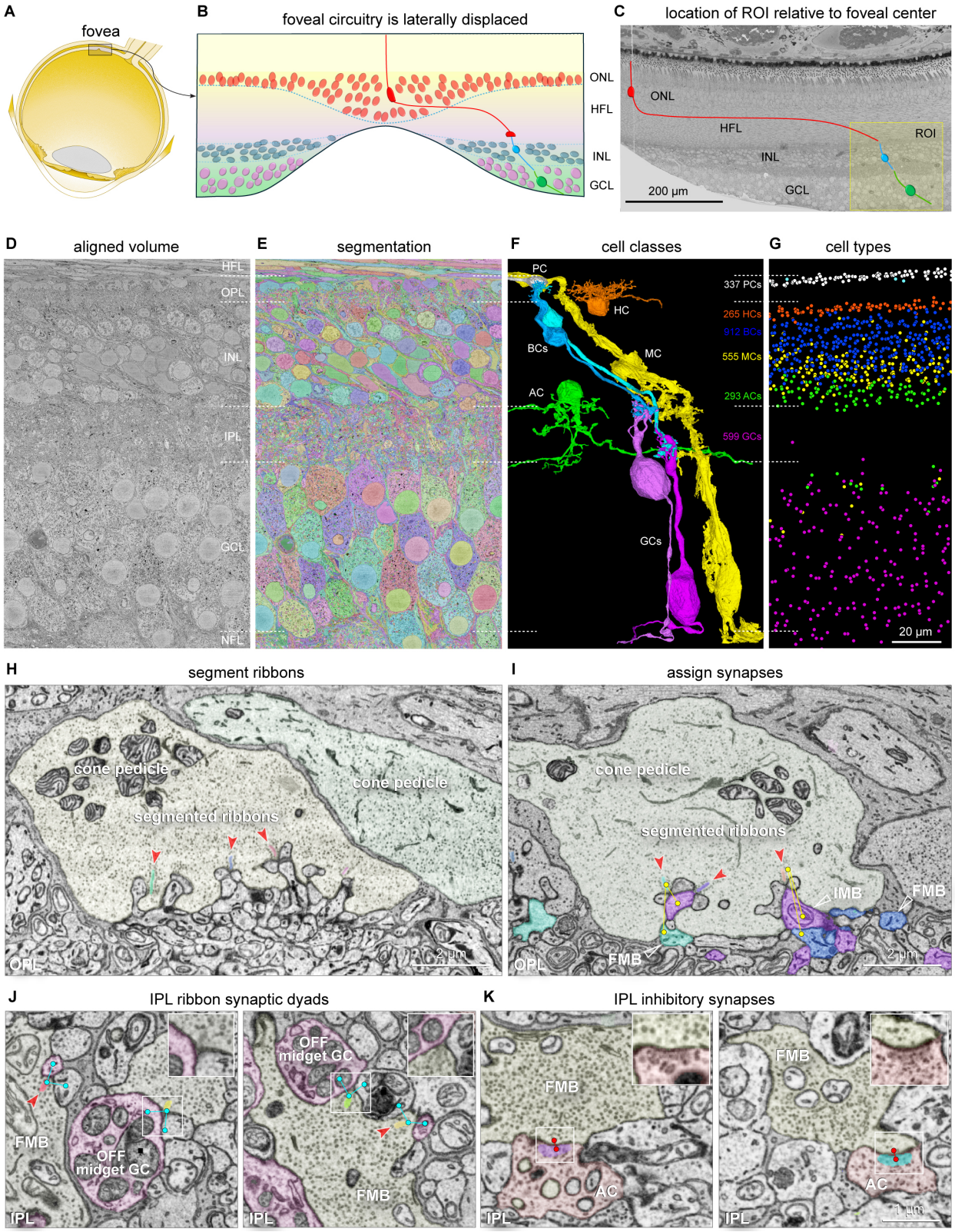
A
fovea
B
foveal circuitry is laterally displaced
ONL
HFL
INL
GCL
C
location of ROI relative to foveal center
ONL
HFL
INL
GCL
ROI
200 µm
D
aligned volume
HFL
OPL
INL
IPL
GCL
NFL
E
segmentation
F
cell classes
PC
HC
BCs
MC
AC
GCs
337 PCs
265 HCs
912 BCs
555 MCs
293 ACs
599 GCs
G
cell types
20 µm
H
segment ribbons
cone pedicle
cone pedicle
segmented ribbons
OPL
2 µm
I
assign synapses
cone pedicle
segmented ribbons
IMB
FMB
FMB
OPL
2 µm
J
IPL ribbon synaptic dyads
FMB
OFF midget GC
IPL
OFF midget GC
FMB
IPL
K
IPL inhibitory synapses
FMB
AC
IPL
FMB
AC
IPL
1 µm

Figure 1

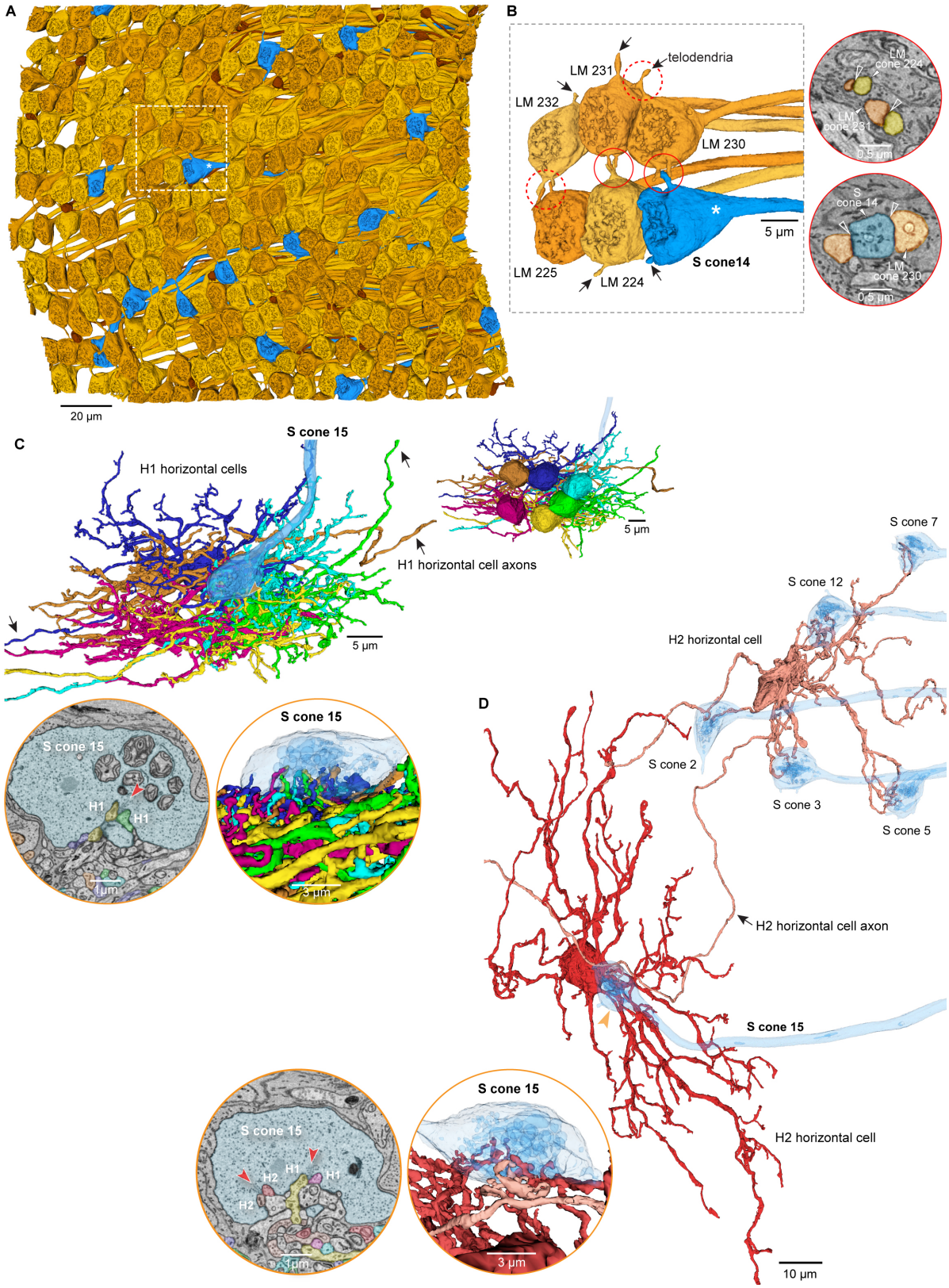
A
20 µm
B
telodendria
LM 231
LM 232
LM 230
LM 225
LM 224
S cone14
5 µm
LM cone 224
LM cone 231
0.5 µm
S cone 14
LM cone 230
0.5 µm
C
S cone 15
H1 horizontal cells
H1 horizontal cell axons
5 µm
5 µm
S cone 15
H1
H1
1 µm
S cone 15
3 µm
D
S cone 7
S cone 12
H2 horizontal cell
S cone 2
S cone 3
S cone 5
H2 horizontal cell axon
S cone 15
H2 horizontal cell
10 µm
S cone 15
H2
H1
H1
H2
1 µm
S cone 15
3 µm

Figure 2

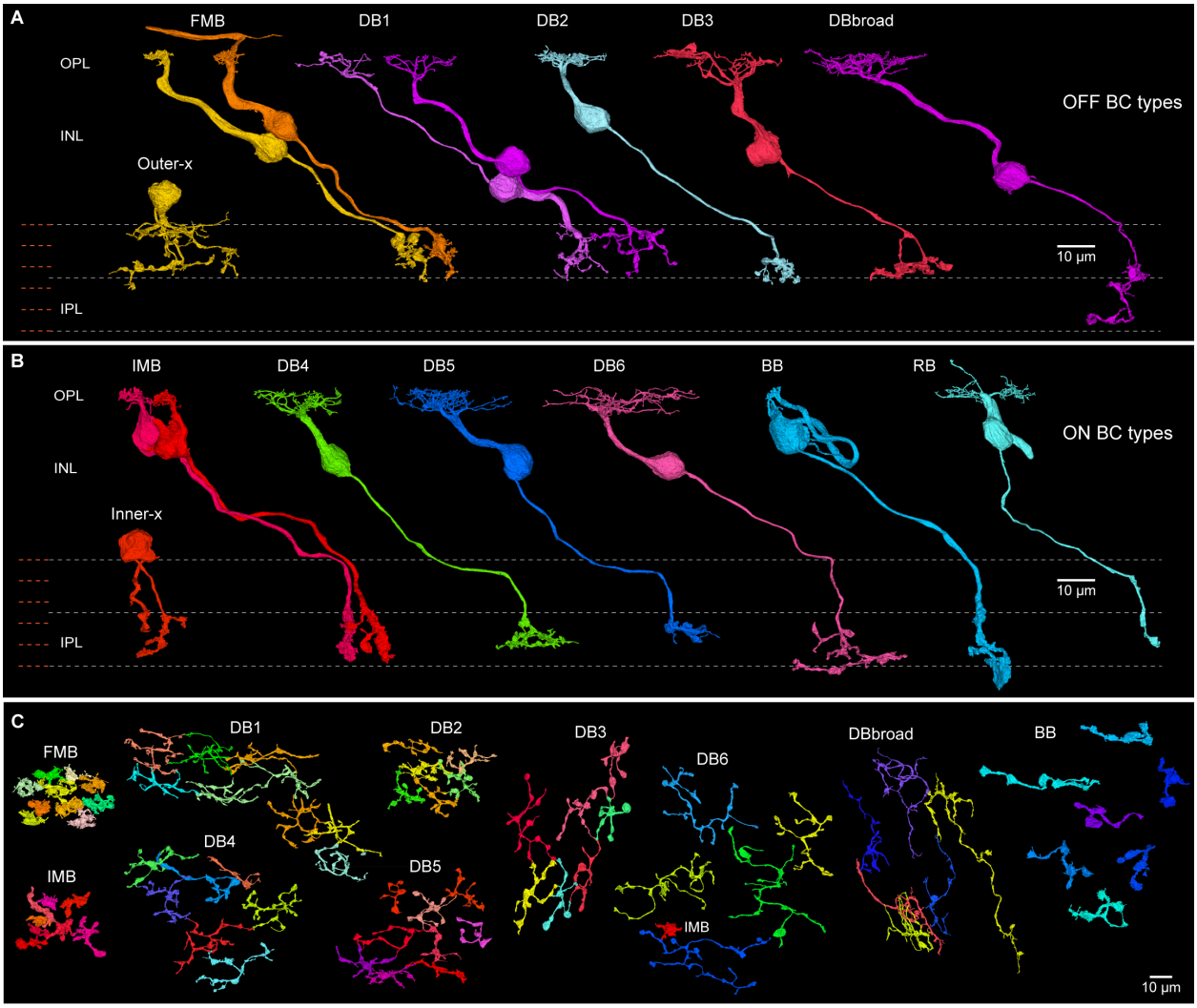
A
FMB
DB1
DB2
DB3
DBbroad
OPL
INL
Outer-x
OFF BC types
10 µm
IPL
B
IMB
DB4
DB5
DB6
BB
RB
OPL
INL
Inner-x
ON BC types
10 µm
IPL
C
FMB
DB1
DB2
DB3
DB6
DBbroad
BB
DB4
IMB
DB5
IMB
10 µm

Figure 3

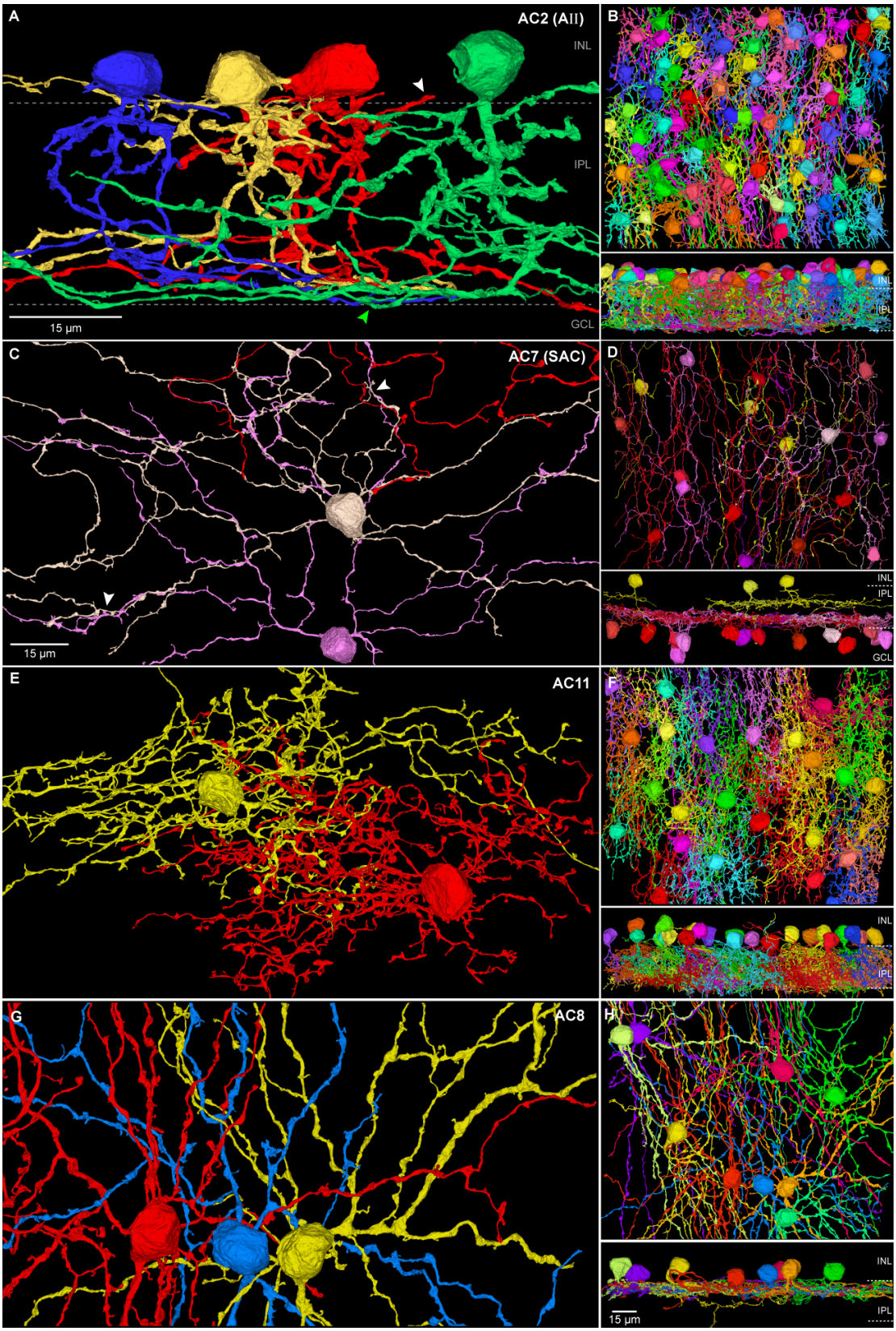

Figure 4

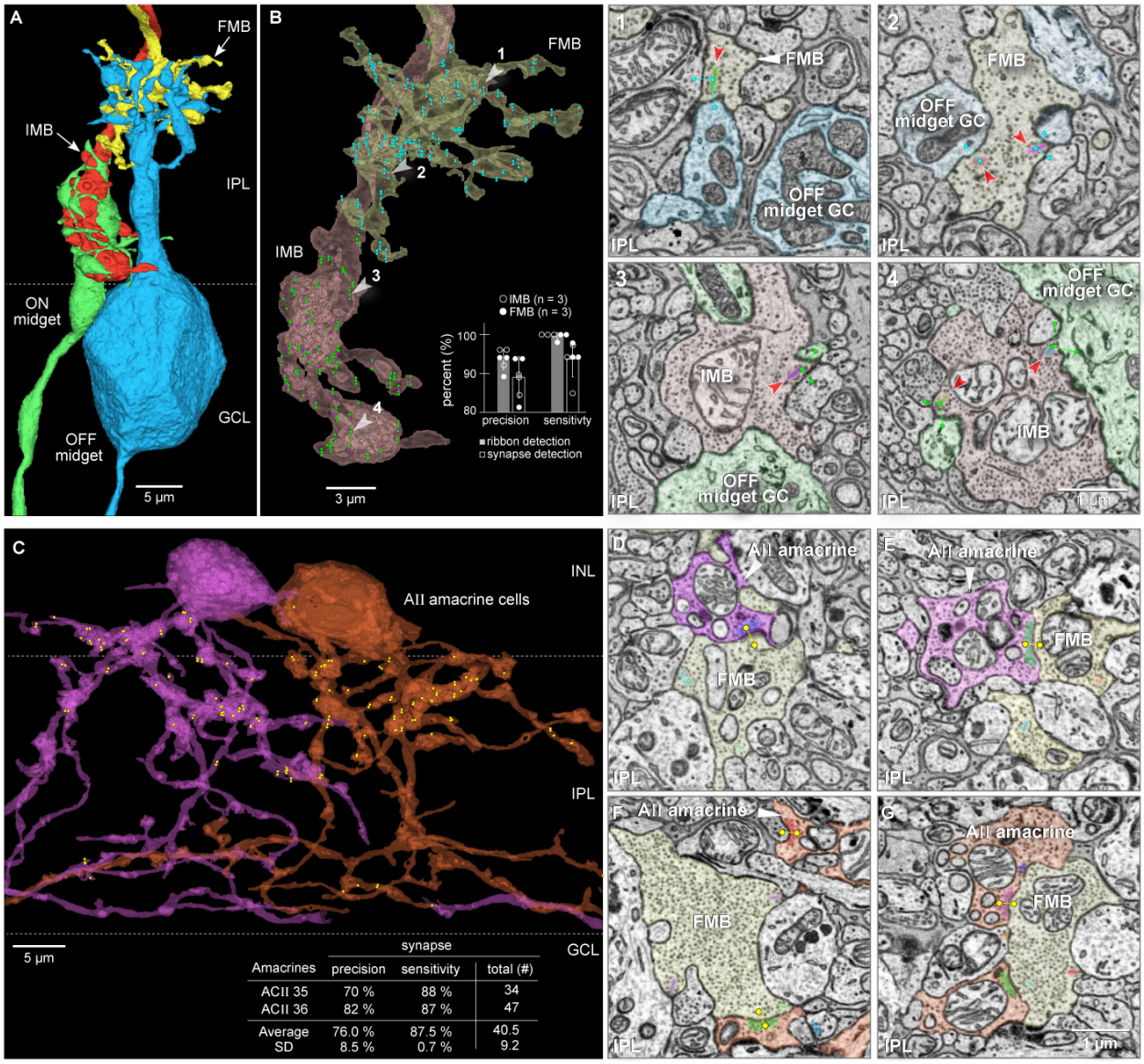

Amacrines	synapse precision	synapse sensitivity	total (#)
ACII 35	70 %	88 %	34
ACII 36	82 %	87 %	47
Average	76.0 %	87.5 %	40.5
SD	8.5 %	0.7 %	9.2

Figure 5

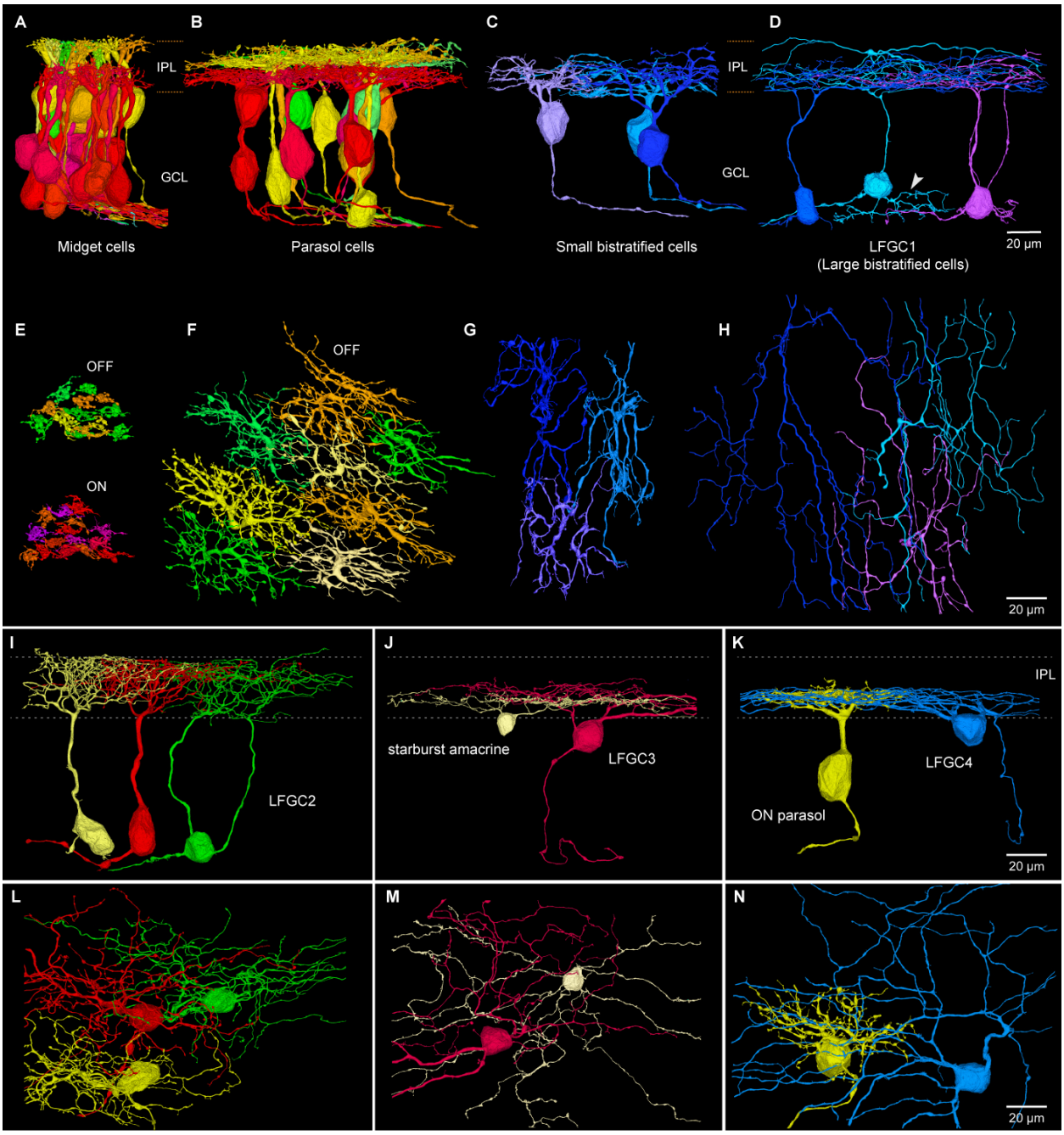
A
B
C
D
IPL
GCL
IPL
GCL
Midget cells
Parasol cells
Small bistratified cells
LFGC1
(Large bistratified cells)
20 µm
E
F
G
H
OFF
ON
OFF
20 µm
I
J
K
IPL
LFGC2
starburst amacrine
LFGC3
LFGC4
ON parasol
20 µm
L
M
N
20 µm

Figure 6

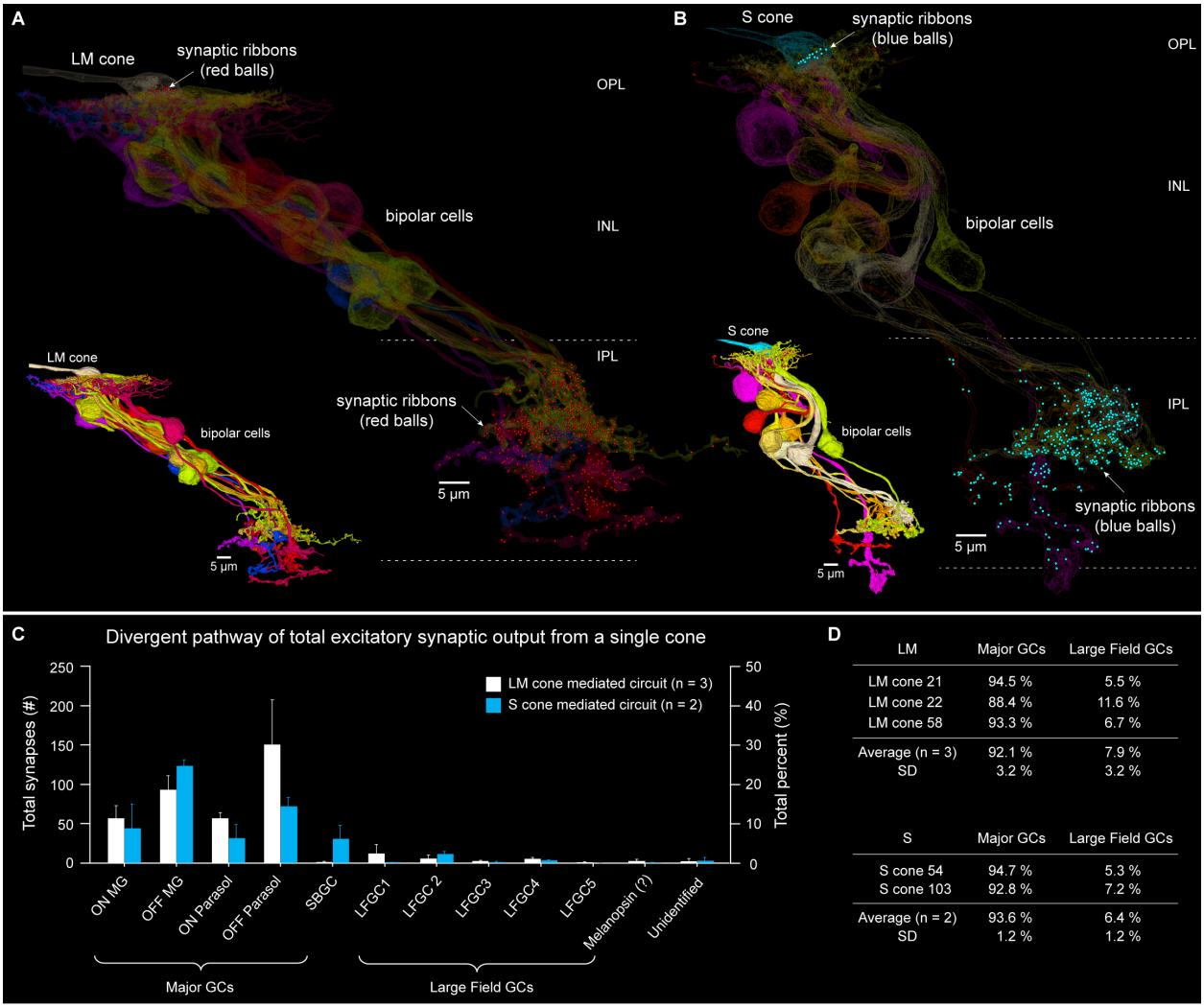

LM	Major GCs	Large Field GCs
LM cone 21	94.5 %	5.5 %
LM cone 22	88.4 %	11.6 %
LM cone 58	93.3 %	6.7 %
Average (n = 3)	92.1 %	7.9 %
SD	3.2 %	3.2 %

S	Major GCs	Large Field GCs
S cone 54	94.7 %	5.3 %
S cone 103	92.8 %	7.2 %
Average (n = 2)	93.6 %	6.4 %
SD	1.2 %	1.2 %

Figure 7